Supporting Information

Deciphering the synergistic role of chemisorbed phosphate on FeOOH for high-efficiency overall water splitting

Xiaoqian Du,[a] Junjun Zhang,*[a] Mengyuan Zhang[a], Huilong Wei[a], Xiu Lin,[c] Wen Guo*[d], Pengfei Zhang,*[a, b] and Zhenghong Luo [a, b]

[a]State Key Laboratory of High-Efficiency Utilization of Coal and Green Chemical Engineering, College of Chemistry and Chemical Engineering, Ningxia University, Yinchuan, Ningxia, 750021, China. E-mail: zhangjj089@nxu.edu.cn; pfzhang@nxu.edu.cn

[b]School of Chemistry and Chemical Engineering, Shanghai Jiao Tong University, Shanghai, 200240, P. R. China. E-mail: chemistryzpf@sjtu.edu.cn

[c]School of Materials Science and Engineering, Nanyang Technological University, 639798, Singapore.

[d]School of Chemistry and Chemical Engineering, State Key Laboratory Incubation Base for Green Processing of Chemical Engineering, Shihezi University, Shihezi, 832003, China. E-mail: wenguo@shzu.edu.cn

List of Contents

Figure S16. CV curves of FeOOH/NIF electrodes at different scan rates from 20 to 100 mV s^{-1} in (a)pure KOH, (b) 0.10 M PO_4^{3-}+1.0 M KOH.

Figure S17. Bode phase plots of the FeOOH/NIF at various potentials in (a)pure KOH, (b) 0.01 M PO_4^{3-}+1.0 M KOH, (c) 0.05 M PO_4^{3-}+1.0 M KOH, (d) 0.15 M PO_4^{3-}+1.0 M KOH and (e) 0.20 M PO_4^{3-}+1.0 M KOH.

Figure S18. Operando Nyquist plots of the FeOOH/NIF at various potentials in (a)pure KOH, (b) 0.01 M PO_4^{3-}+1.0 M KOH, (c) 0.05 M PO_4^{3-}+1.0 M KOH, (d) 0.15 M PO_4^{3-}+1.0 M KOH and (e) 0.20 M PO_4^{3-}+1.0 M KOH.

Figure S19. The long-time E-t curve of the FeOOH/NIF in 0.10 M PO_4^{3-}+1.0 M KOH for OER (j=50 mA cm^{-2}).

Figure S20. (a) The LSV curves, (b) EIS Nyquist plots for FeOOH/NIF electrode before and after 1000 CV cycles.

Figure S21. Chronoamperometry curves with multiple steps for the FeOOH/NIF electrode in 0.10 M PO_4^{3-}+1.0 M KOH.

Figure S22. Chronopotentiometry curves with multiple steps for the FeOOH/NIF electrode in 0.10 M PO_4^{3-}+1.0 M KOH.

Figure S23. LSV curves for HER of samples with various soaking times in 1.0 M KOH.

Figure S24. LSV curves for HER of samples with various soaking times in 1.0 M KOH+0.10 M PO_4^{3-}.

Figure S25. LSV curves of NIF for HER at different PO_4^{3-} concentrations.

Figure S26. EIS plots of NIF for HER at different PO_4^{3-} concentrations.

Figure S27. Comparison of LSV curves for HER for FeOOH/NIF and FeOOH+NIF in 0.10 M PO_4^{3-} + 1.0 M KOH.

Figure S28. CV curves of FeOOH/NIF electrodes at different scan rates from 20 to 100 mV s^{-1} in (a)pure KOH, (b) 0.10 M PO_4^{3-}+1.0 M KOH.

Figure S29. Comparison of FeOOH/NIF overpotentials at different PO_4^{3-} concentrations at (a) -100 mA cm^{-2} and (b) -200 mA cm^{-2}.

Figure S30. Bode phase plots of the FeOOH/NIF at various potentials in pure KOH.

Figure S31. Operando Nyquist plots of the FeOOH/NIF at various potentials in pure KOH.

Figure S32. Comparison of LSV curves for HER between FeOOH/NIF and commercial catalyst

1. Experiment Section

1.1 Materials

$FeCl_3$ (Aladdin, ≥ 98%), NaCl (Adamas, ≥ 99.9%), $K_3PO_4 \cdot 3H_2O$ (Damao, ≥ 99.0%), IrO_2 (Macklin, ≥ 99.9%), anhydrous ethanol (99.9%), hydrochloric acid (37%), deionized water. All chemicals were used as received without further purification.

1.2 Substrate preparation

Slice the acquired Nickel-iron foam (NIF) into 1 cm × 3 cm rectangular segments. Immerse the segments in a pre-prepared 3 $mol \cdot L^{-1}$ hydrochloric acid solution. Perform ultrasonic cleaning for 20-30 minutes. Once the cleaning process is finished, rinse the NIF repeatedly with deionized water and absolute ethanol until the solution's pH = 7. Finally, use filter paper to promptly remove any residual moisture and ethanol from the surface of the treated NIF.

1.3 Preparation of FeOOH/NIF electrodes

The preparation procedure of the catalyst follows our previously reported protocol. [1, 2] 5 mmol of $FeCl_3$ and 20 mmol of NaCl were dissolved in 50 mL deionized water, heated, and magnetically until boiling occurred. The pretreated NIF was then immersed in the solution for 60 s. The electrode was rinsed three times with water and ethanol, dried at 60 °C for 12 h in a vacuum oven, resulting in FeOOH/NIF with a catalyst loading of 1.17 mg cm^{-2}. The resultant powder was centrifuged, washed three times with water and ethanol, and dried overnight at 60 °C.

1.4 Preparation of IrO_2/NIF and Pt/C/NIF electrodes

5.0 mg of Pt/C was placed in a 1.5 mL centrifuge tube. Then, 320 μL deionized water, 640 μL absolute ethanol, and 40 μL Nafion dispersion were added using a pipette. The mixture was sonicated for 1 h. The prepared ink was applied drop-by-drop (58.5 μL) to a 1 cm×1 cm NIF, with 15-minute drying intervals after each of four applications. Finally, the coated Pt/C/NIF was dried at 60°C for 2 h. The preparation process of the IrO_2/NIF electrode was similar to the above method.

1.5 Electrochemical characterizations

Electrochemical performance tests were performed at room temperature using an electrochemical workstation (DH7000C, Donghua, China). FeOOH/NIF, IrO_2/NIF or Pt/C/NIF as working electrode, graphite rod and standard Hg/HgO electrode as counter electrode and reference electrode, 1.0 M KOH+ 0.10 M K_3PO_4 as electrolyte.

At the initiation of the OER experiment, the catalyst was subjected to 20 cycles of cyclic

voltammetry (CV) at 10 mV s^{-1} within the voltage range of 0.5-1.2 V vs. Hg/HgO to stabilize the catalyst surface. The oxygen evolution performance of the catalyst was determined by linear sweep voltammetry (LSV) in the range of 0-1.2 V vs. Hg/HgO. Double layer capacitance (C_{dl}) measurements were conducted by varying the scan rates (20, 40, 60, 80, 100 mV/s) in a potential window nearly without Faradaic process. The polarization curves were established as overpotential vs log current (log j) to get Tafel plots for evaluating the OER reaction kinetics of obtained catalysts. By fitting the Tafel plots (the linear portion) to the Tafel equation ($\eta = b\log(j) + a$), the Tafel slope was obtained. The electrochemical impedance spectroscopy (EIS) test was performed in the frequency range of 0.1-1000 Hz, and the in-situ impedance of the catalyst was measured using EIS in the range of 0.40-0.80 V vs. Hg/HgO. In the range of 0.5-1.2 V, 1000 CV cycles were carried out at a scan rate of 50 mV s^{-1}. The stability of the catalyst was evaluated by comparing the LVS and EIS before and after 1000 CV cycles. The stability of the catalyst was tested at 50 mA cm^{-2} and 100 mA cm^{-2}. At the same time, multi-step currents 20, 40, 60, 80, and 100 mA cm^{-2} and multi-step potential 0.55, 0.60, 0.65, 0.70, 0.75 and 0.8 V were used to evaluate the stability of the catalyst in the dynamic current and potential.

At the commencement of the HER experiment, the catalyst was subjected to 20 cycles of CV of 10 mV/s within the -0.6 to -2.2V range to stabilize the catalyst surface. The HER performance was ascertained through LSV within the range of -0.6 to -2.2V vs. Hg/HgO. The EIS test covered a frequency range of 0.1-1000 Hz at -1.1 V vs. Hg/HgO. The long-term stability was examined -50 mA cm^{-2} and -100 mA cm^{-2}.

The conditions for water electrolysis involved a 1.0 M KOH+0.10 M PO_4^{3-} solution, utilizing FeOOH/NIF as the working electrode in a two-electrode system at 1-2V. The stability was tested at current densities of 50 mA cm^{-2} and 100 mA cm^{-2}.

1.6 Material characterizations

The X-ray diffraction (XRD) patterns were recorded on a Rigaku MiniFlex 600-C X-ray diffractometer with Cu-Kα radiation with a scan rate of 5° min^{-1}. The Scanning electron microscopy (SEM) characterizations were conducted using a JSM-7800F from JEOL. Transmission electron microscopy (TEM) and high-resolution transmission electron microscopy (HRTEM) measurements were taken with a JEOL JEM-F200 microscope operated. The X-ray photoelectron spectroscopy (XPS) measurements were conducted on a Kratos Axis Ultra DLD spectrometer.

1.7 In-situ Raman measurements

Raman measurements were conducted employing a Raman JY HR800 (wavenumber range of 200-1200 cm^{-1}) coupled with an in-situ Raman flow cell (EC-Raman, Beijing Scistar Technology, China). A 50× long working distance objective (8 mm) was utilized, and the excitation laser, with a wavelength of 532 nm, originated from a He-Ne laser with an approximate power of 6 mW. Calibration of the Raman frequency was achieved using a Si wafer. Data acquisition involved Raman readings at various constant potentials (1.15-1.65 V vs. RHE and -0.38 to -1.08 V vs. RHE), with a stabilization period of 20 seconds preceding each measurement. FeOOH/NIF as the working electrode, while the counter electrode and reference electrode for Raman measurement comprised a carbon rod and Hg/HgO, respectively. 1.0 M KOH and 1.0 M KOH + 0.10 M PO_4^{3-} electrolyte solution was utilized.

1.8 Computational details

All density functional theory calculations were performed using the Perdew-Burke-Ernzerhof formulation within the generalized gradient approximation.[3, 4] These calculations were conducted with the Vienna Ab Initio Package.[5] The wave function was expressed with the plane wave basis set and a cut-off energy of 400 eV was used. The structures were fully relaxed until the energy and force converged to 1×10^{-6} eV and 0.02 eV/Å, respectively. The calculations use a 3×3×1 k-point grid for Brillouin zone sampling. The DFT-D3 semiempirical correction was described via Grimme's scheme method. The adsorption energy (E_{ads}) of adsorbate A was defined as: $E_{ads} = E_{A*surf} - E_{surf} - E_A$, where E_{A*surf} represents the energy of the adsorbate A adsorbed on the surface, E_{surf} and E_A is the energy of isolated A molecule in a cubic periodic box, respectively. The free energy of gas-phase molecules or surface adsorbates is calculated from the equation $G = E+ZPE-TS$, where E is the total energy, ZPE is the zero-point energy, T is the temperature in Kelvin (298.15 K is set here), and S is the entropy.

2. Supplementary Figures

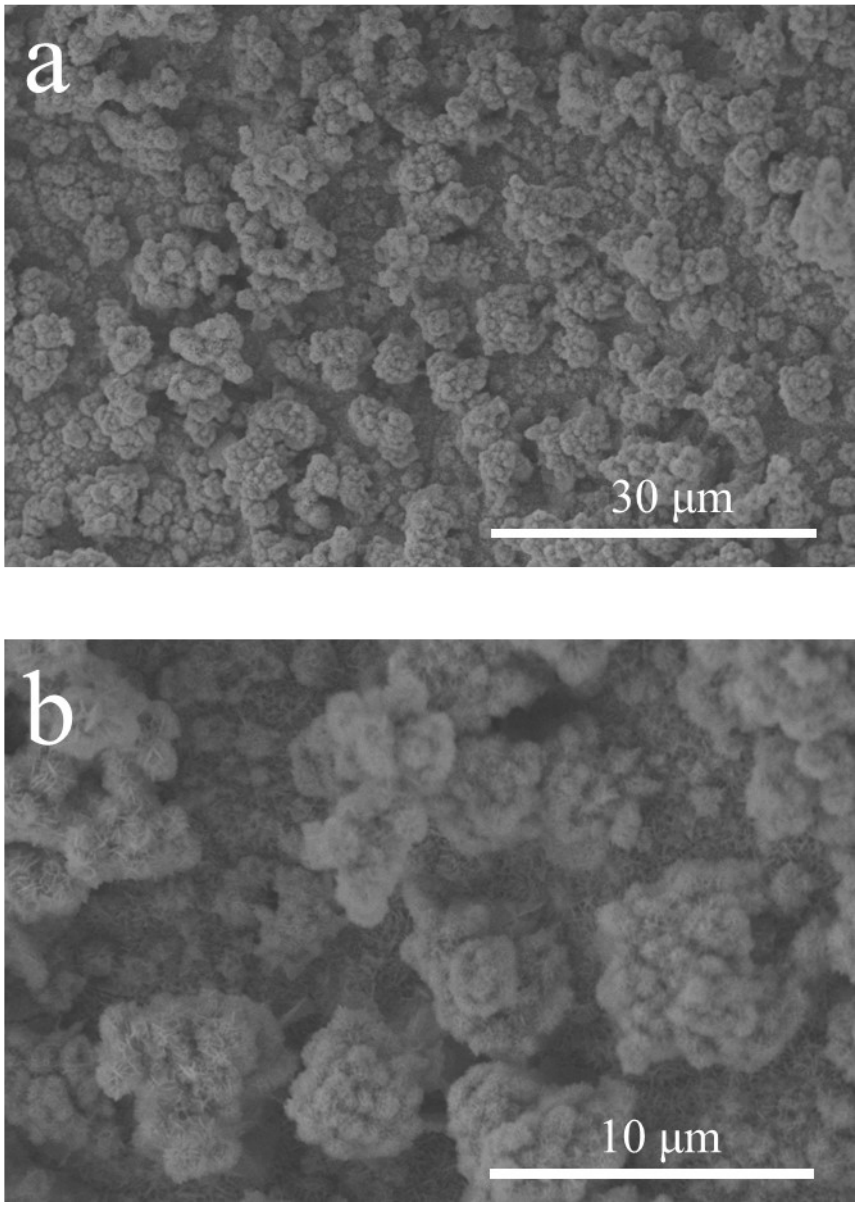

Figure S1. SEM images of FeOOH/NIF at various magnifications.

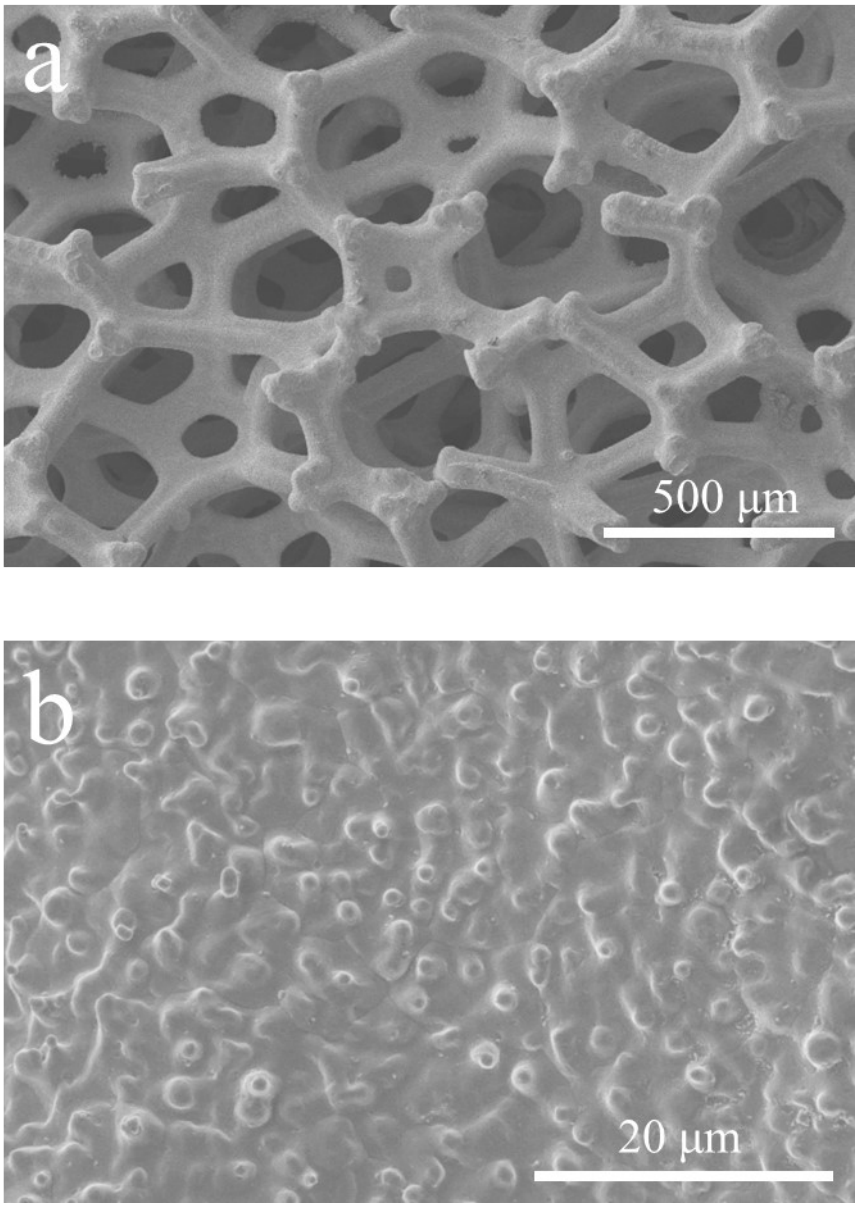

Figure S2. SEM images of NIF at various magnifications.

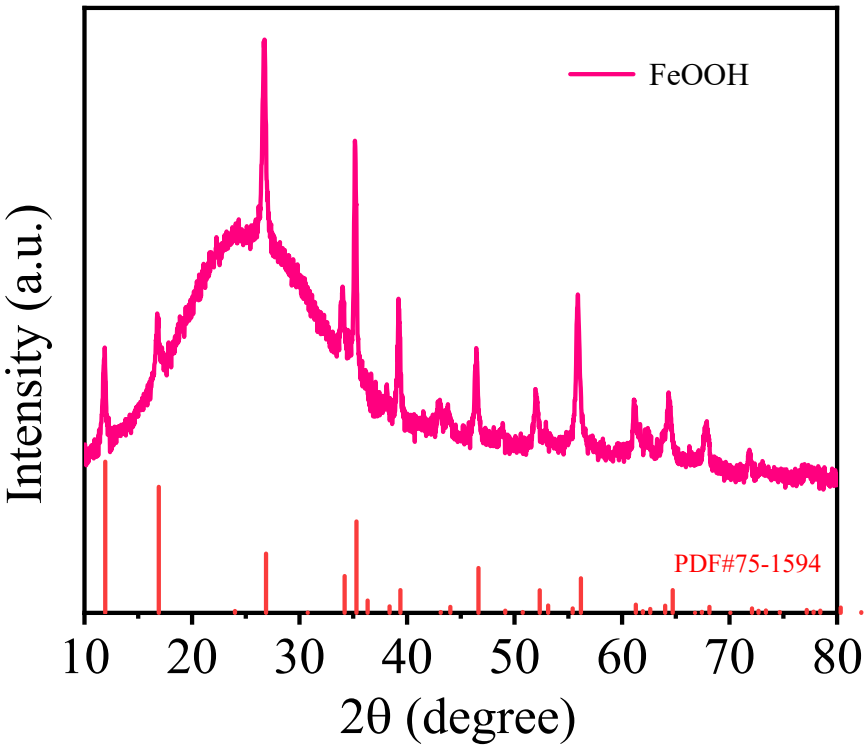

Figure S3. XRD pattern of FeOOH.

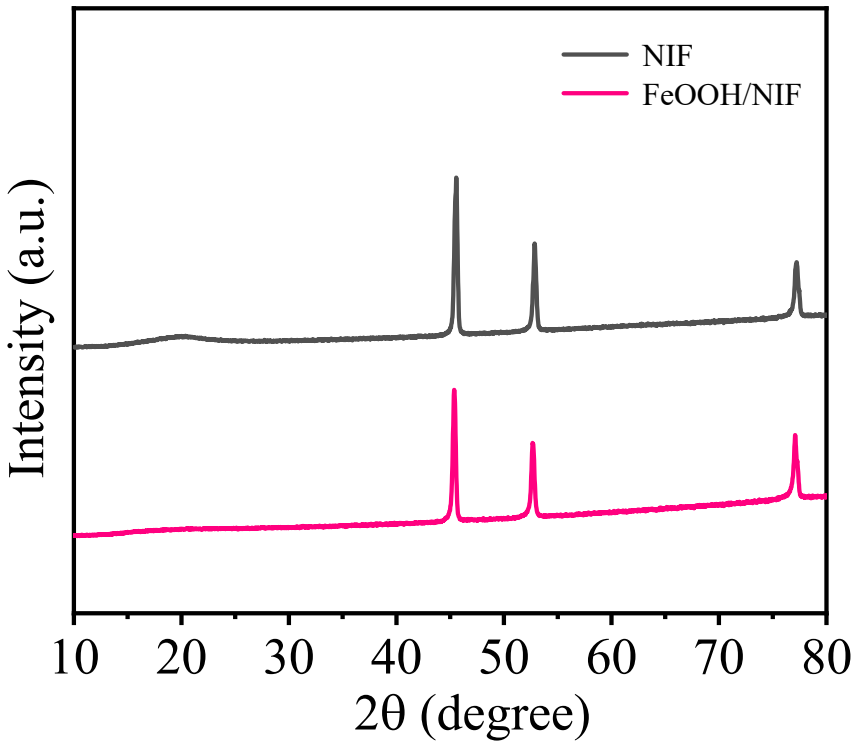

Figure S4. XRD patterns of NIF and FeOOH/NIF.

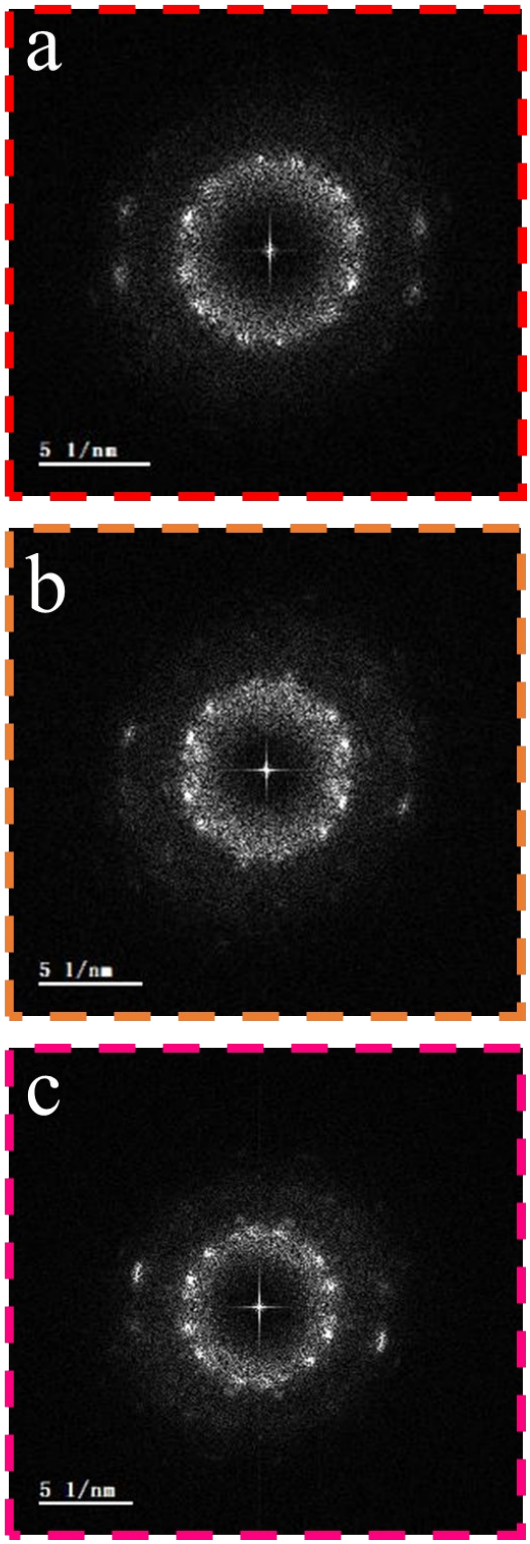

Figure S5. FFT plots within the respective rectangular regions (Figure 2e).

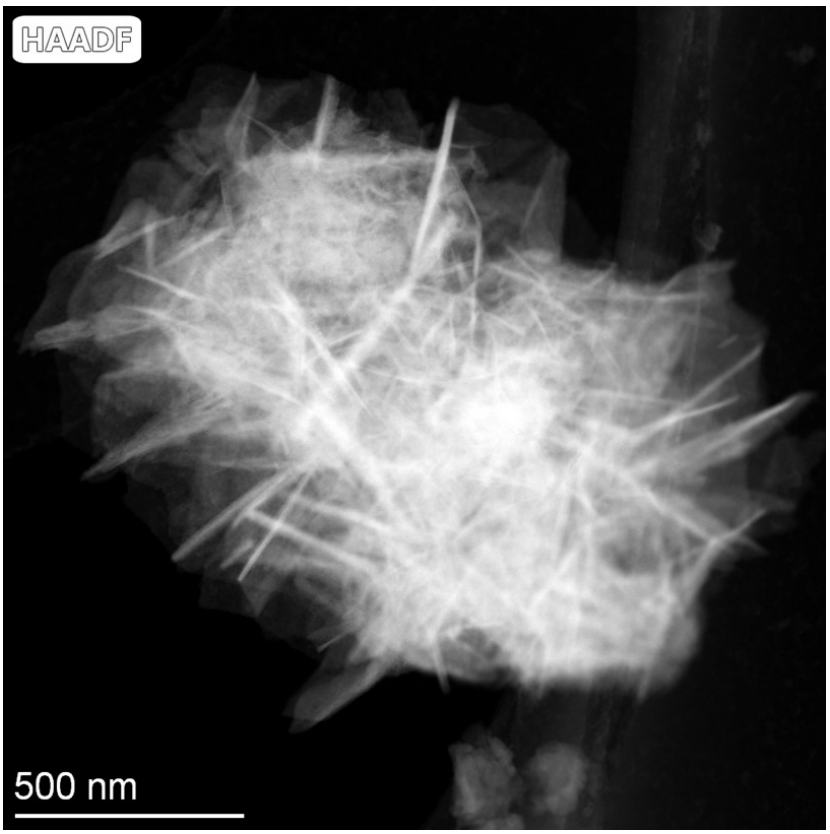

Figure S6. The HAADF-STEM of FeOOH/NIF.

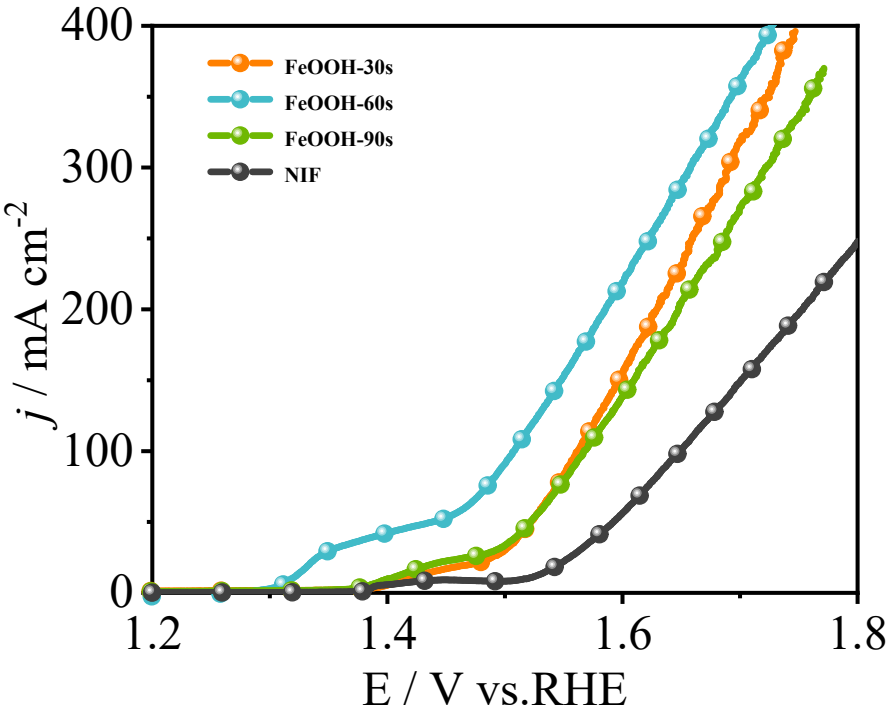

Figure S7. LSV curves of samples with various soaking times in 1.0 M KOH.

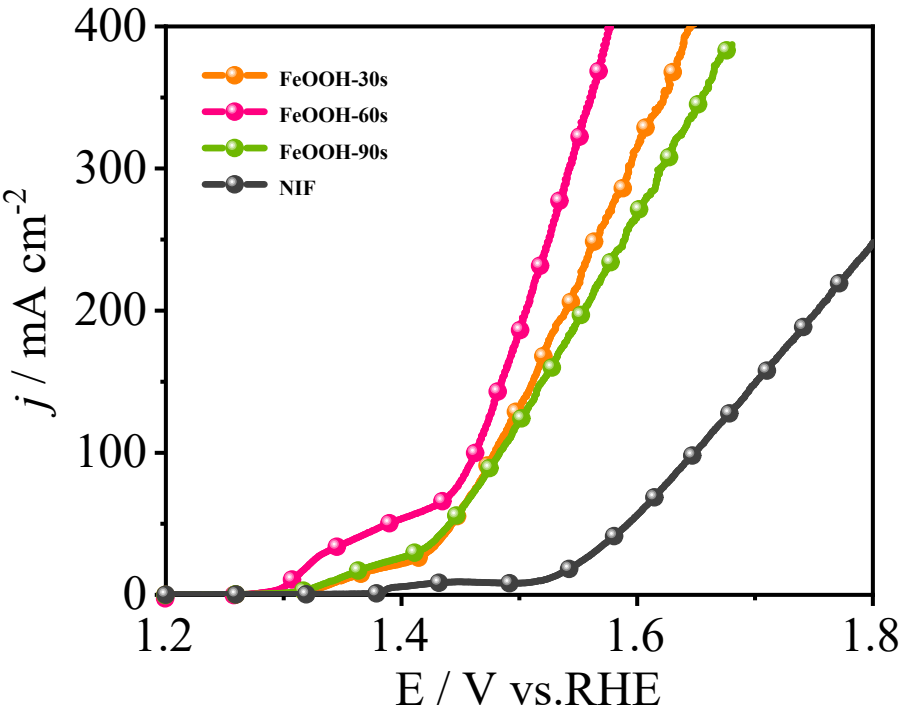

Figure S8. LSV curves of samples with various soaking times in 1.0 M KOH+0.10 M PO_4^{3-}.

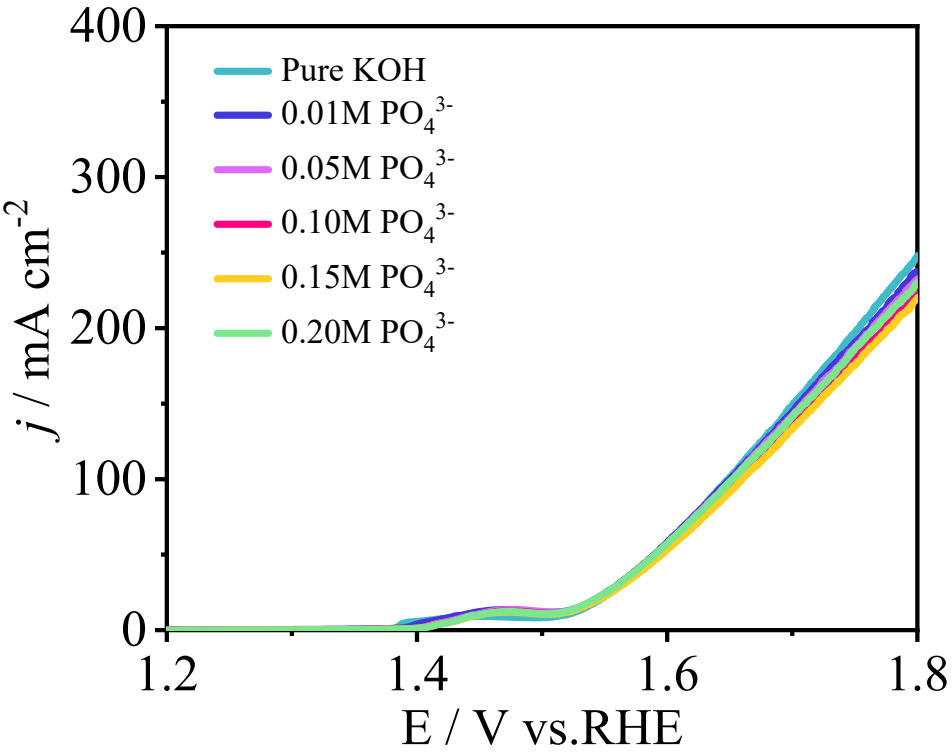

Figure S9. LSV curves of NIF under varying concentrations of PO_4^{3-}.

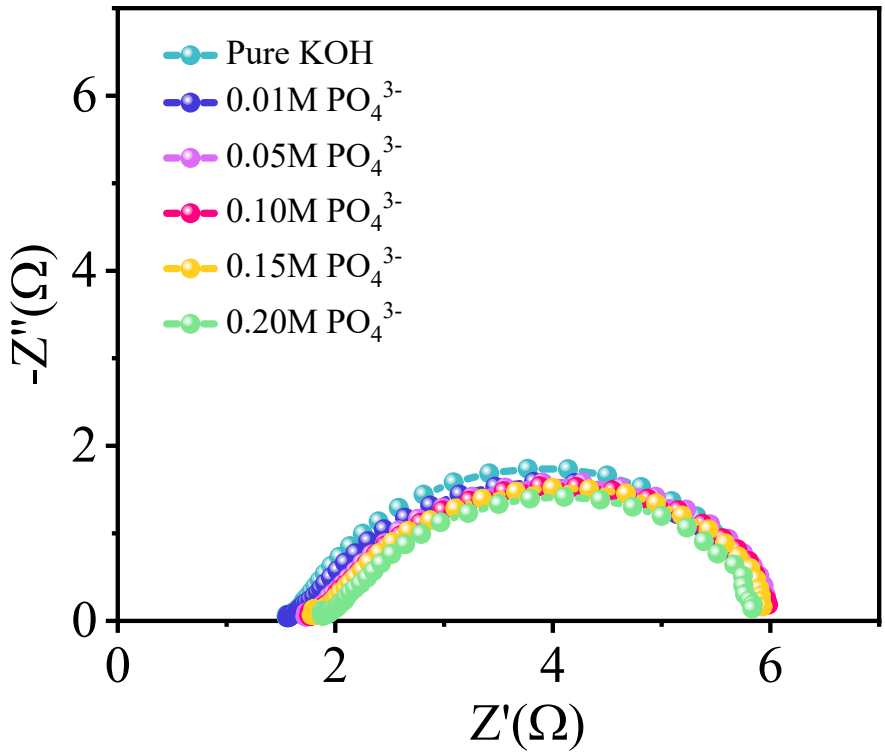

Figure S10. EIS plots of NIF under varying concentrations of PO_4^{3-}.

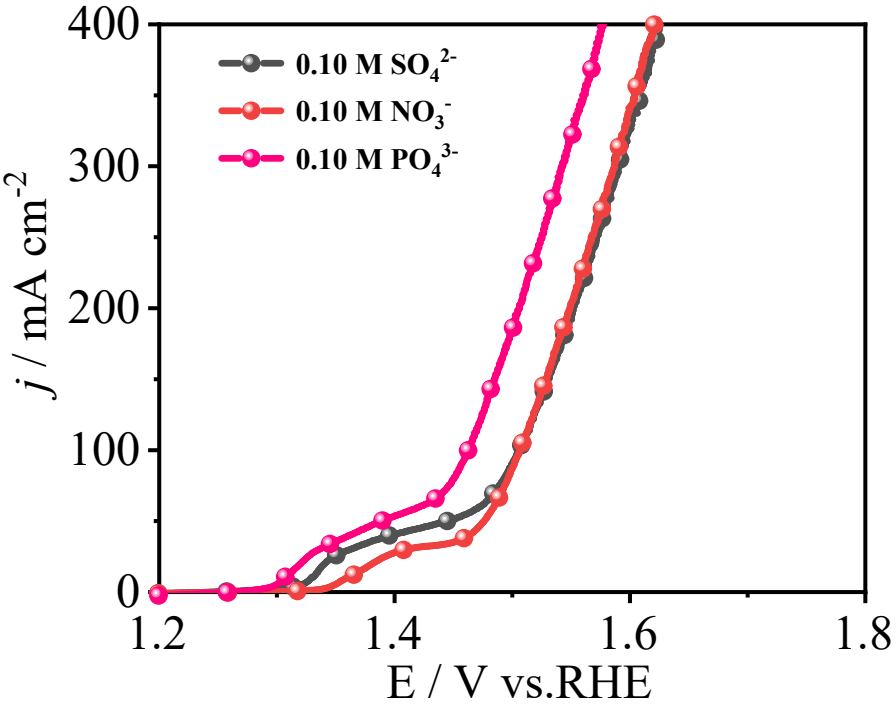

Figure S11. LSV curves of FeOOH/NIF in different oxygen anions.

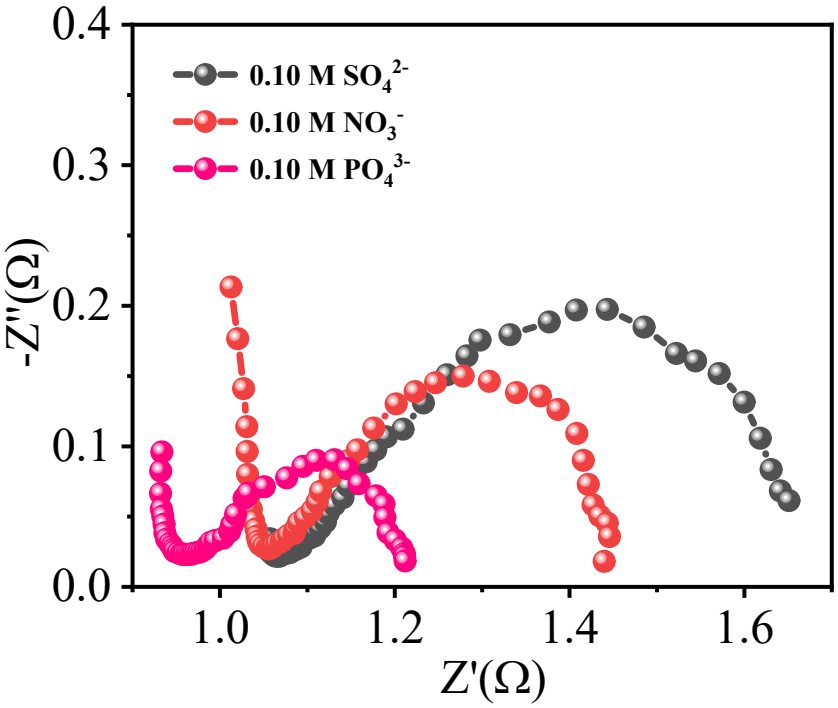

Figure S12. EIS plots of FeOOH/NIF in different oxygen anions.

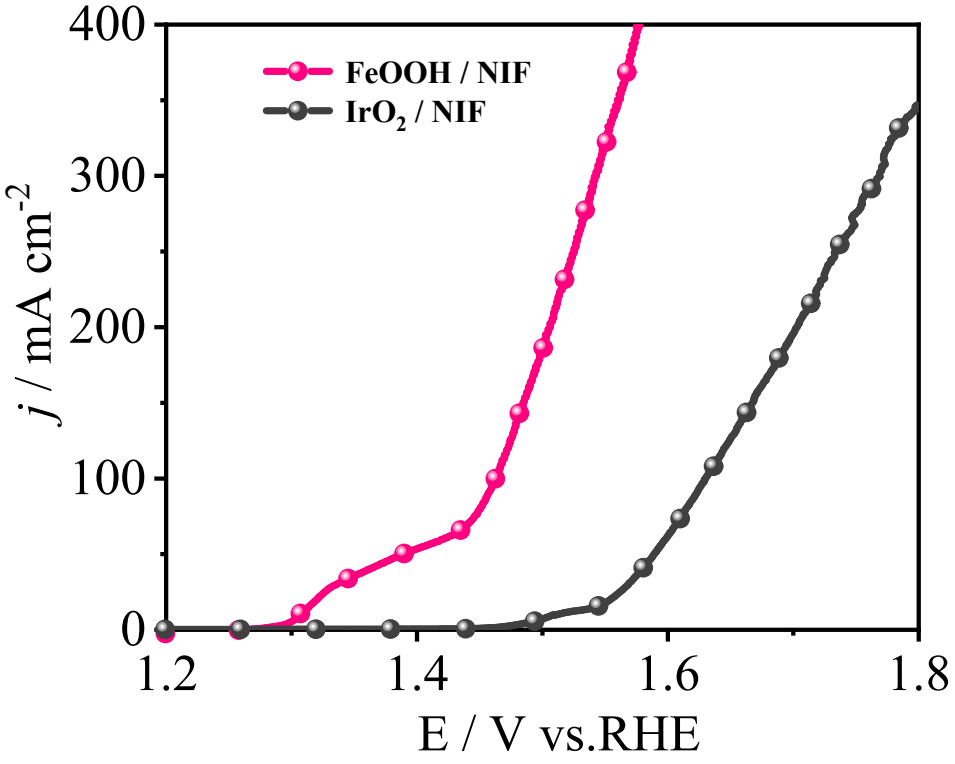

Figure S13. Comparison of LSV curves for FeOOH/NIF and IrO_2/NIF in 0.10 M PO_4^{3-} + 1.0 M KOH.

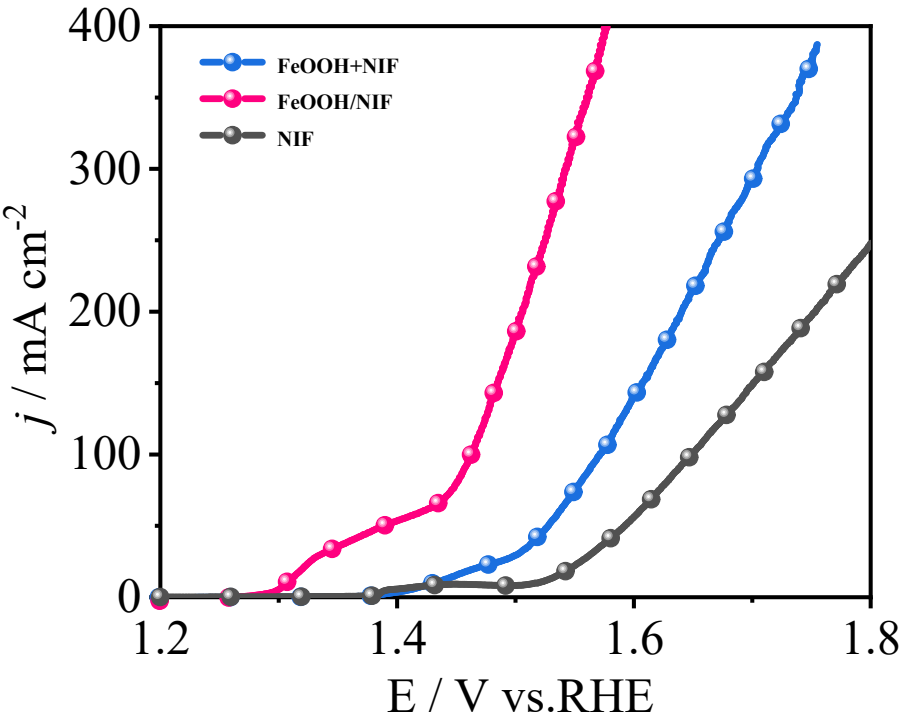

Figure S14. Comparison of LSV curves for FeOOH/NIF and FeOOH+NIF in 0.10 M PO_4^{3-} + 1.0 M KOH.

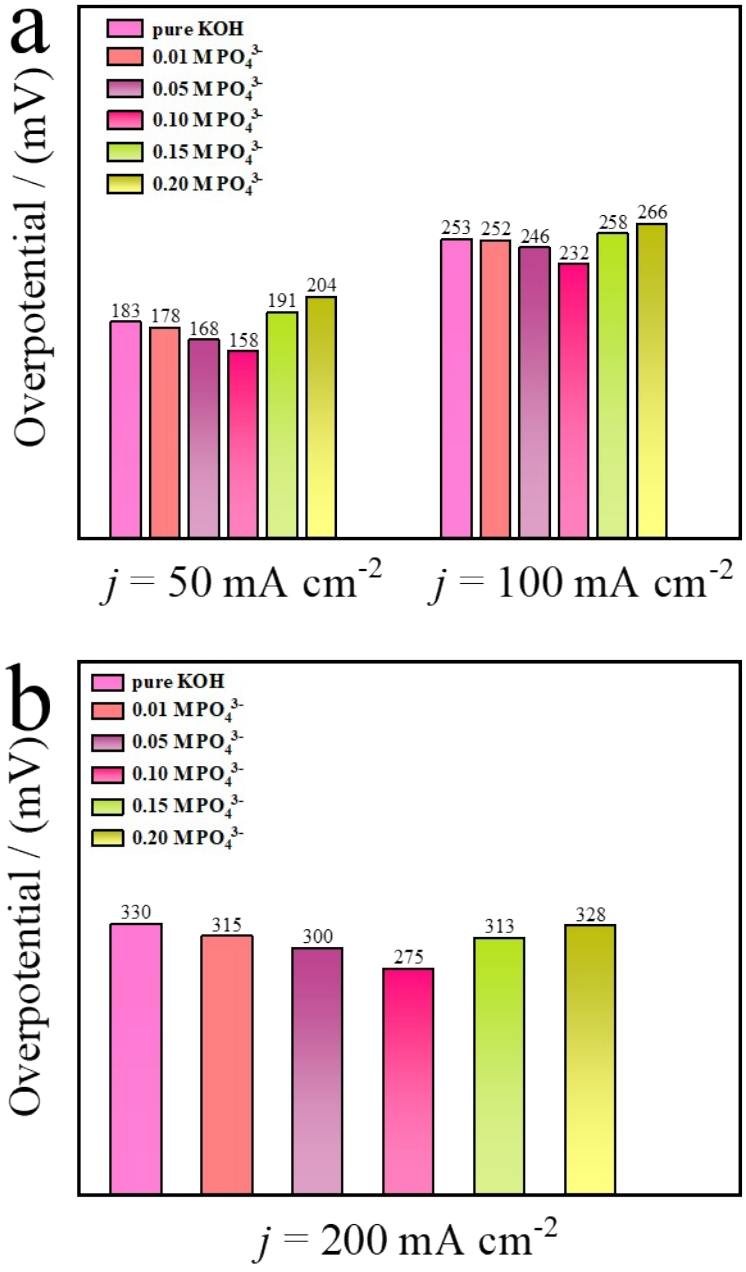

Figure S15. (a) Comparison of FeOOH/NIF overpotentials in different PO_4^{3-} concentrations at 50 and 100 mA cm^{-2}. (b) Comparison of FeOOH/NIF overpotentials in different PO_4^{3-} concentrations at 200 mA cm^{-2}.

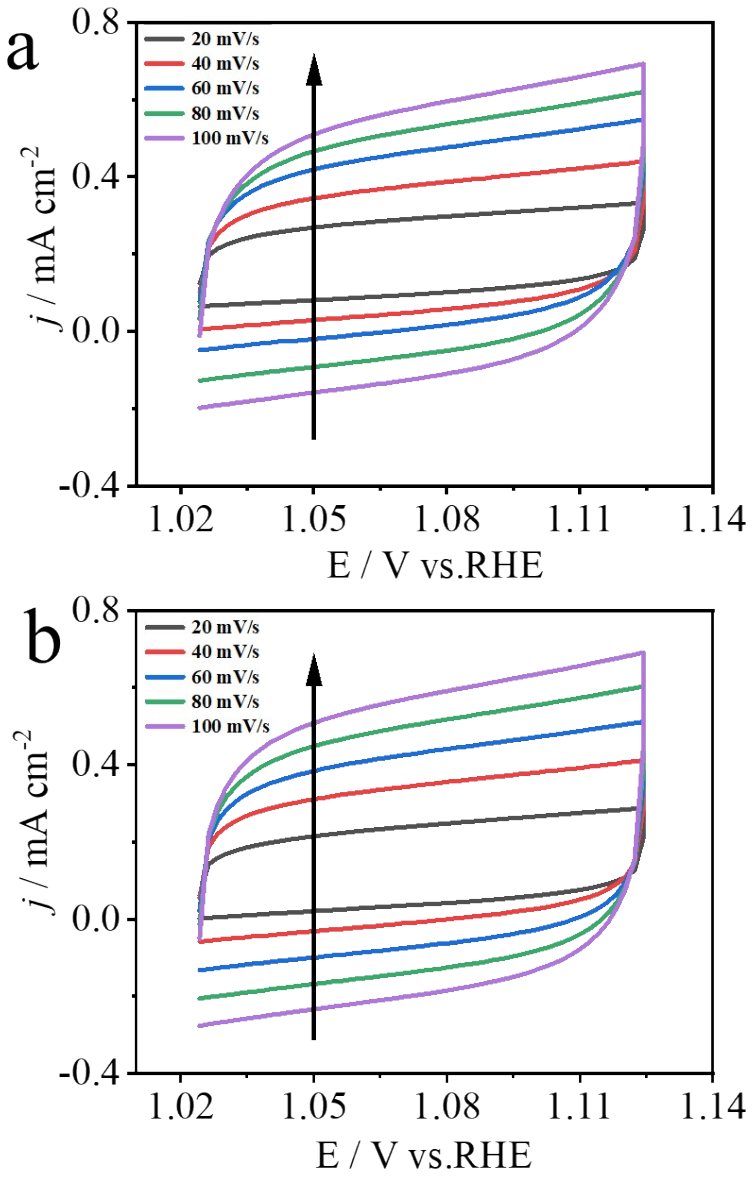

Figure S16. CV curves of FeOOH/NIF electrodes at different scan rates from 20 to 100 mV s^{-1} in (a) pure KOH, (b) 0.10 M PO_4^{3-}+1.0 M KOH.

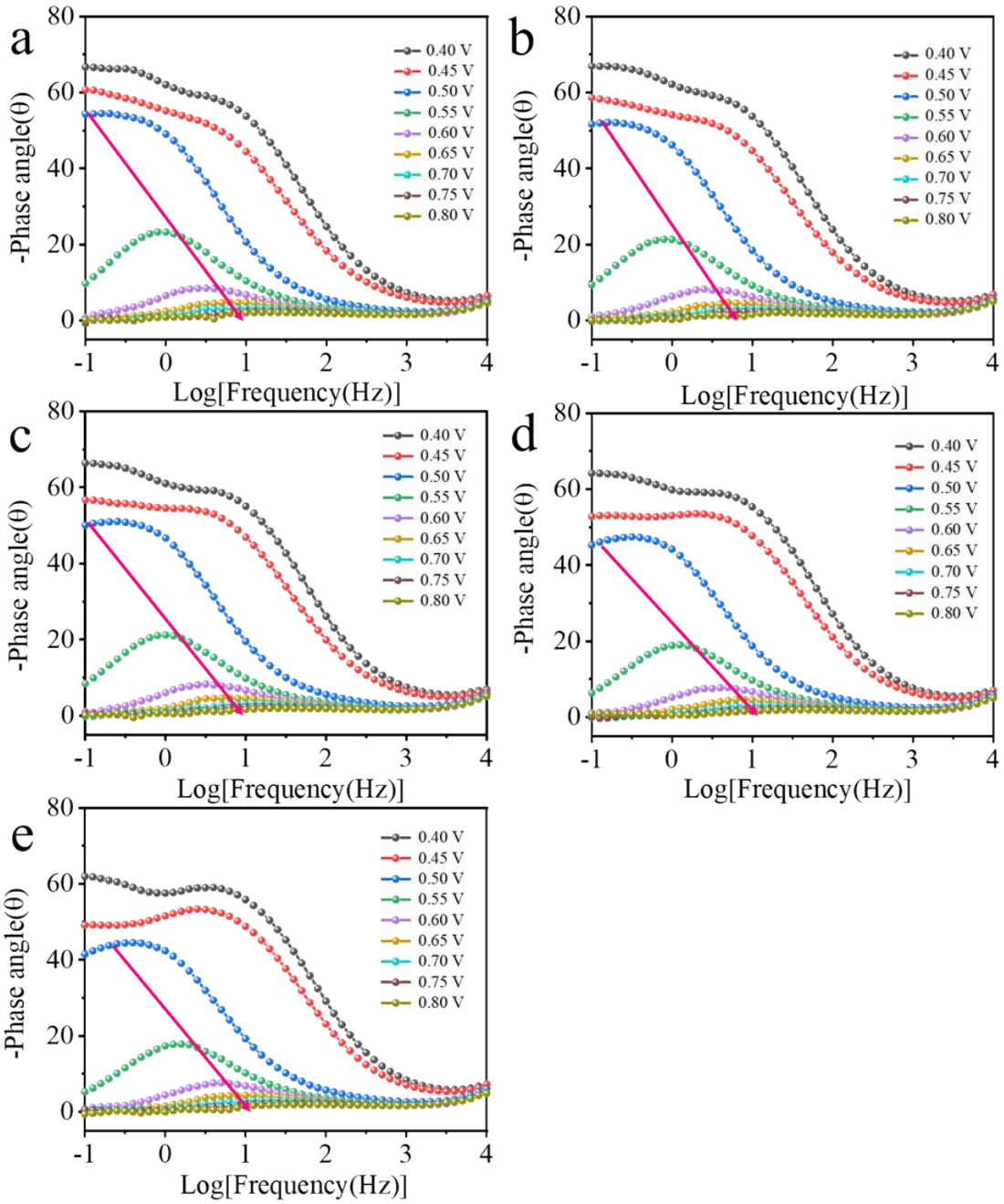

Figure S17. Bode phase plots of the FeOOH/NIF at various potentials in (a)pure KOH, (b) 0.01 M PO_4^{3-}+1.0 M KOH, (c) 0.05 M PO_4^{3-}+1.0 M KOH, (d) 0.15 M PO_4^{3-}+1.0 M KOH and (e) 0.20 M PO_4^{3-}+1.0 M KOH.

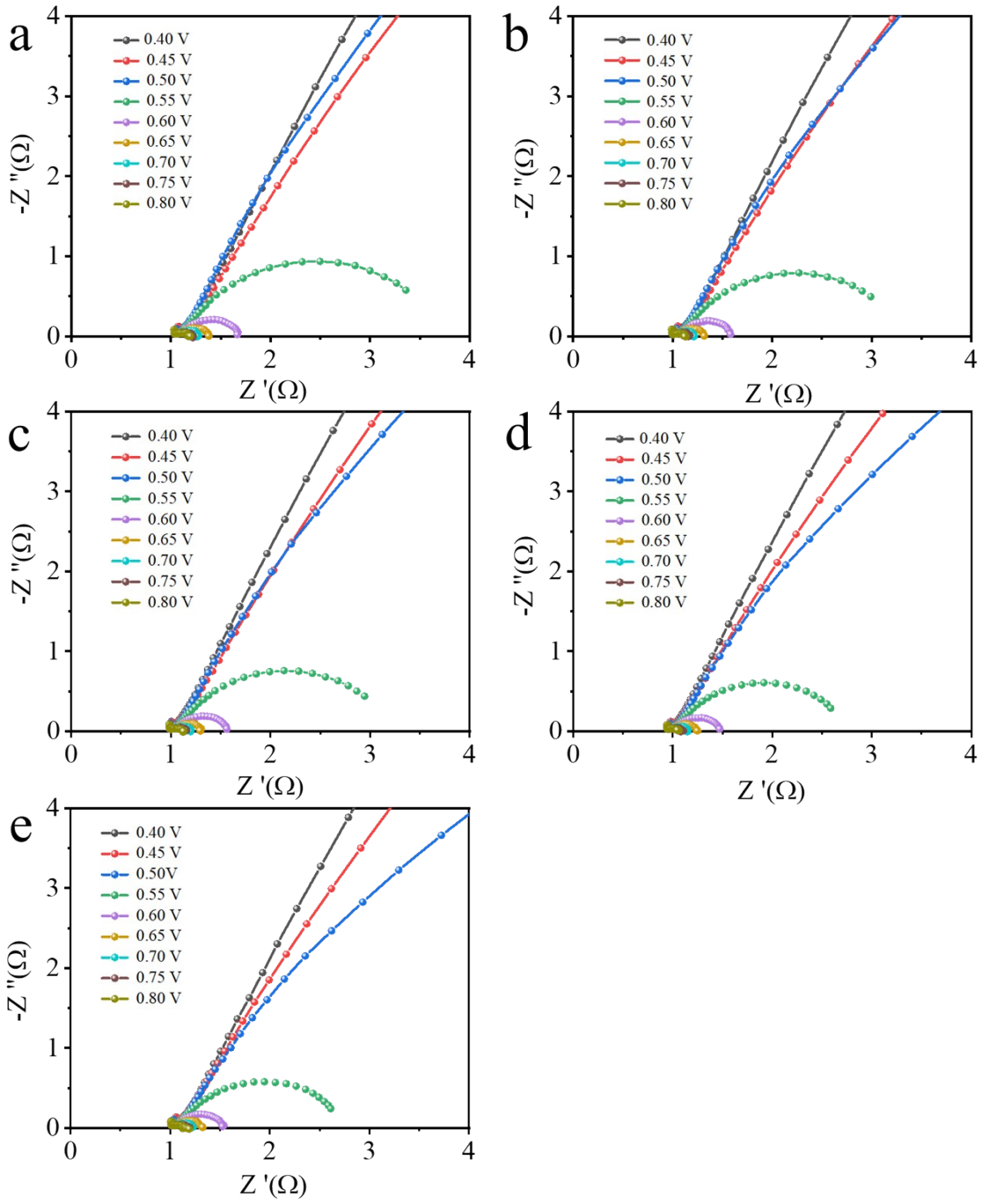

Figure S18. Operando Nyquist plots of the FeOOH/NIF at various potentials in (a) pure KOH, (b) 0.01 M PO_4^{3-}+1.0 M KOH, (c) 0.05 M PO_4^{3-}+1.0 M KOH, (d) 0.15 M PO_4^{3-}+1.0 M KOH and (e) 0.20 M PO_4^{3-}+1.0 M KOH.

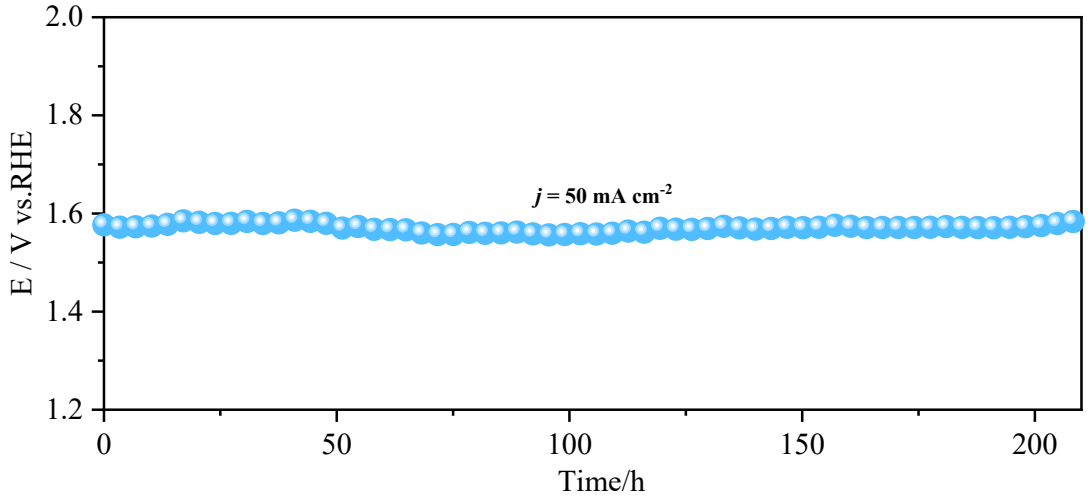

Figure S19. The long-time E-t curve of the FeOOH/NIF in 0.10 M PO_4^{3-}+1.0 M KOH for OER (j=50 mA cm^{-2}).

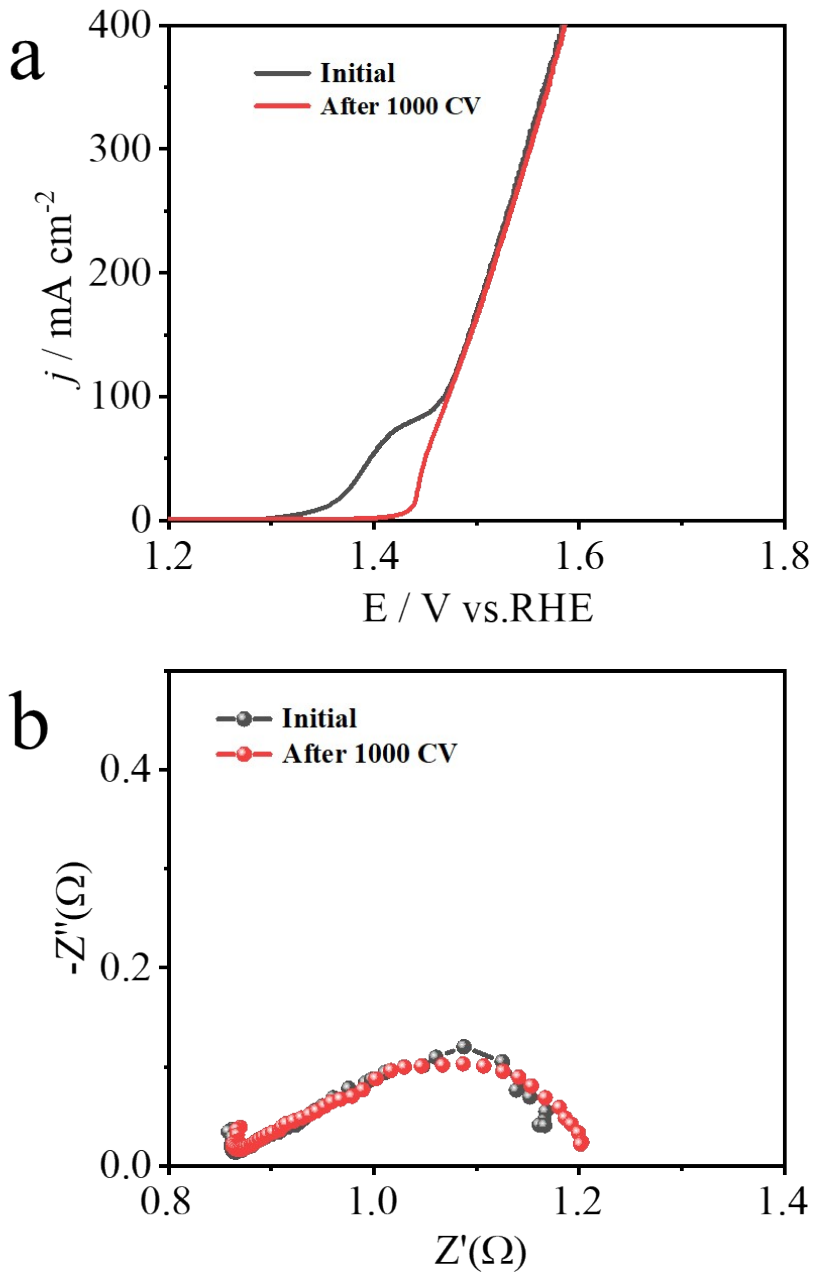

Figure S20. (a) The LSV curves, (b) EIS Nyquist plots for FeOOH/NIF electrode before and after 1000 CV cycles.

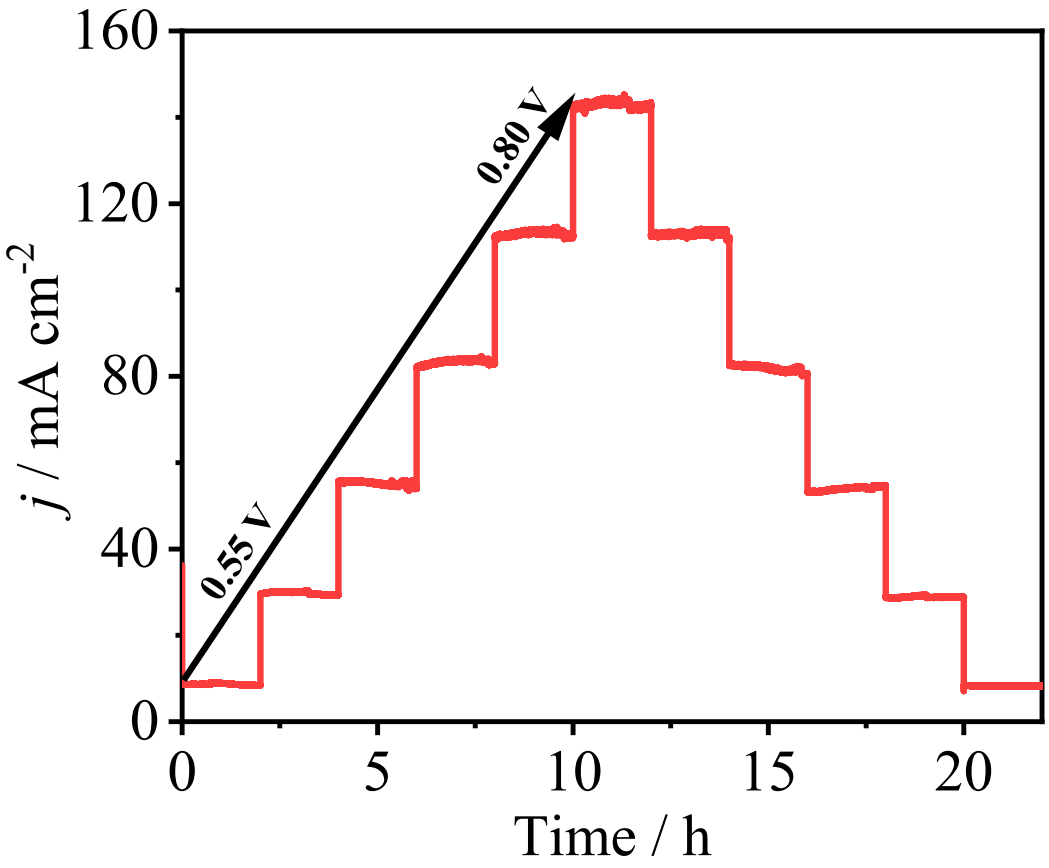

Figure S21. Chronoamperometry curves with multiple steps for the FeOOH/NIF electrode in 0.10 M PO_4^{3-}+1.0 M KOH.

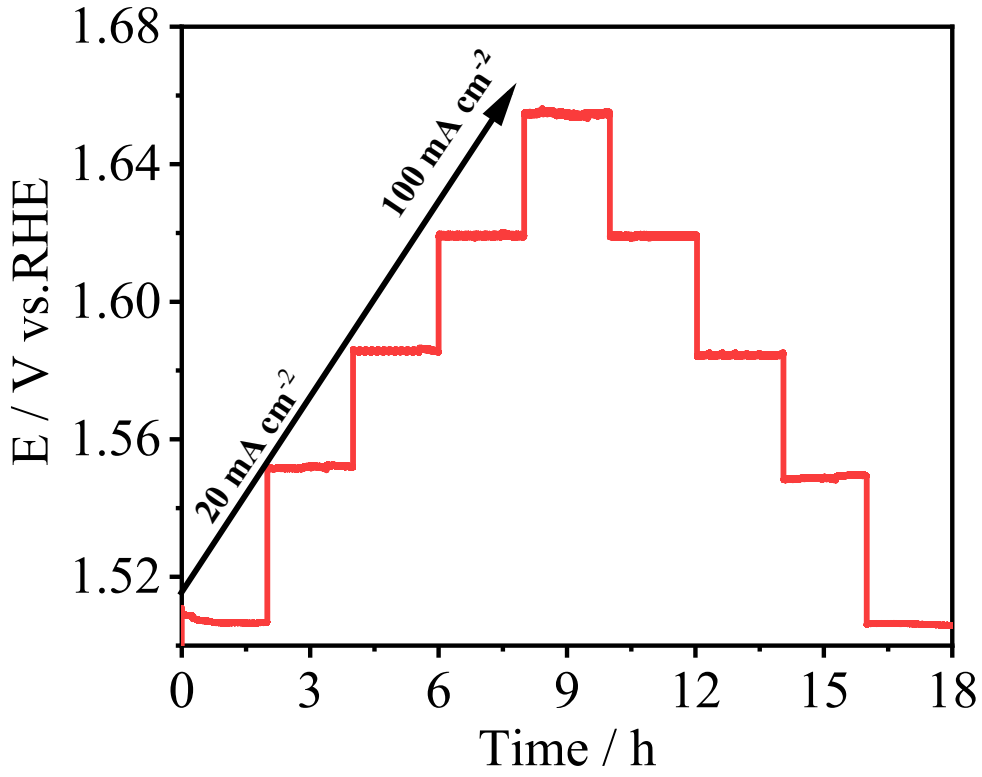

Figure S22. Chronopotentiometry curves with multiple steps for the FeOOH/NIF electrode in 0.10 M PO_4^{3-}+1.0 M KOH.

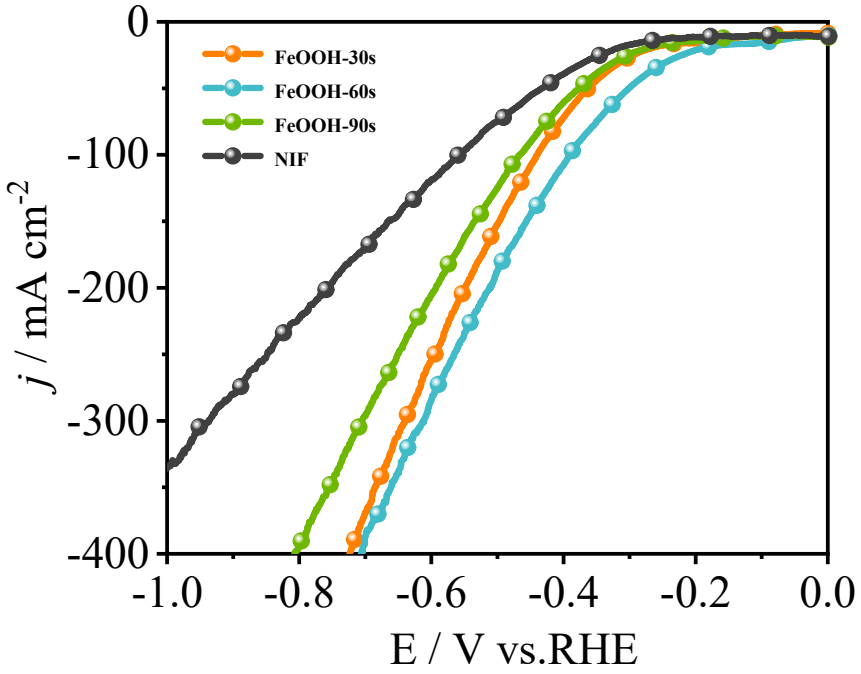

Figure S23. LSV curves for HER of samples with various soaking times in 1.0 M KOH.

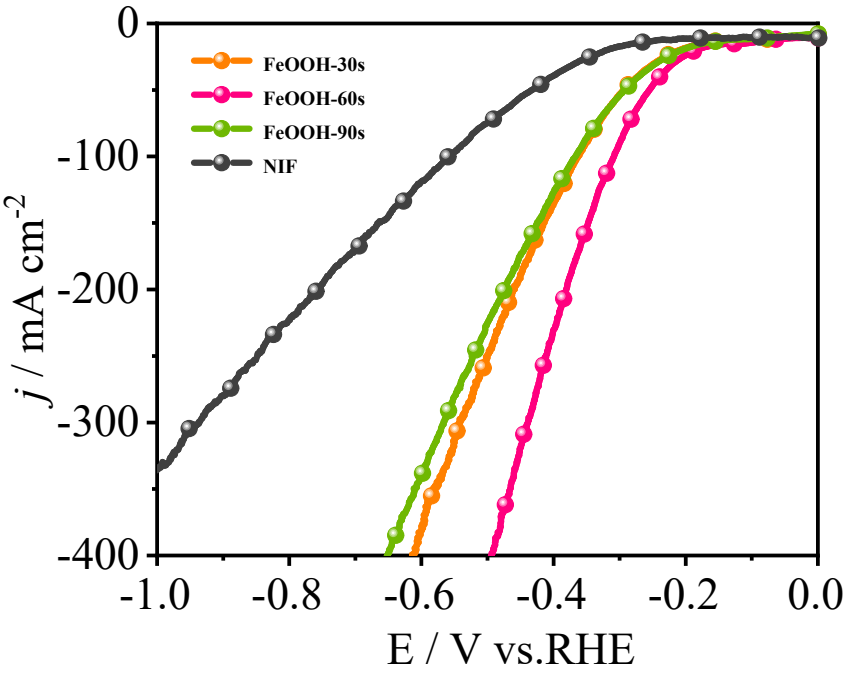

Figure S24. LSV curves for HER of samples with various soaking times in 1.0 M KOH+0.10 M PO_4^{3-}.

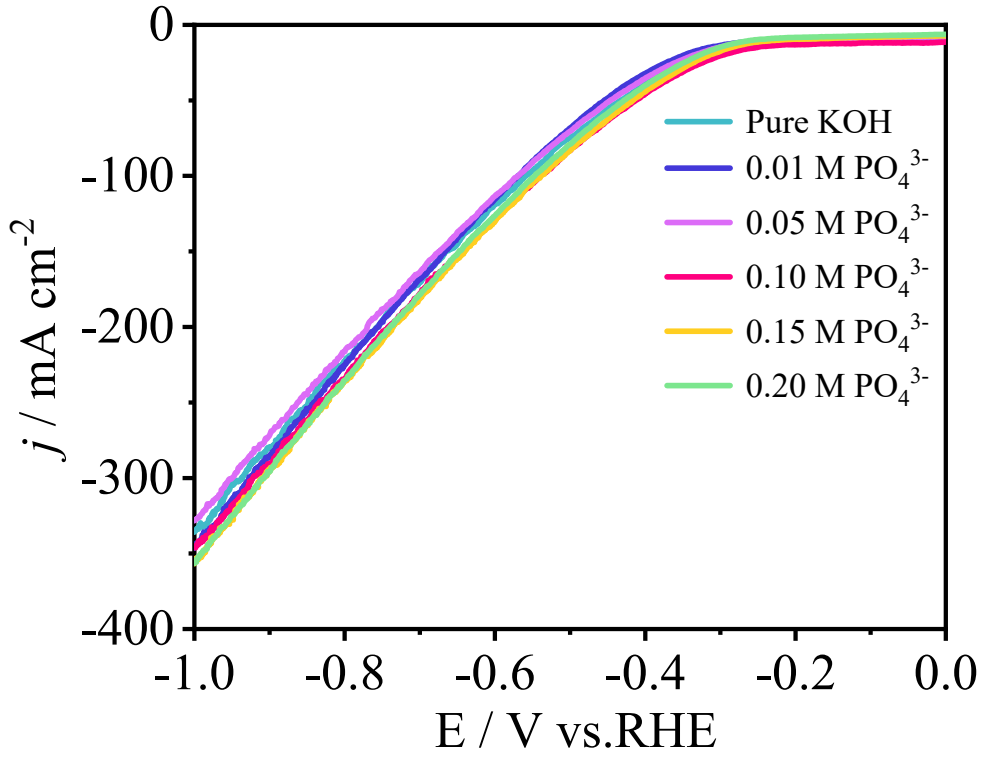

Figure S25. LSV curves of NIF for HER at different PO_4^{3-} concentrations.

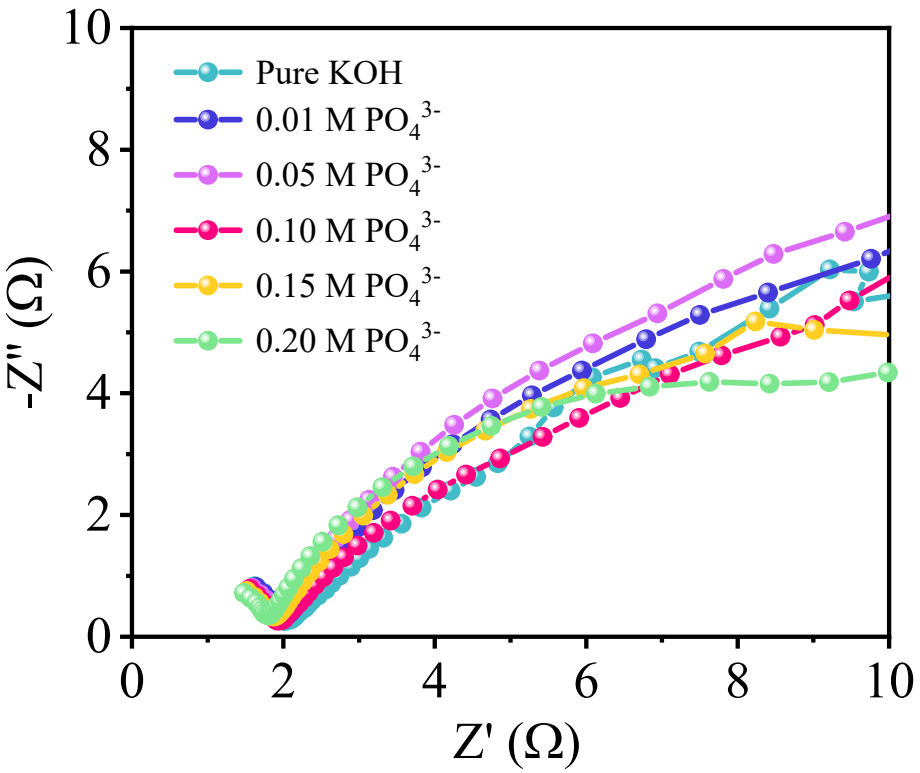

Figure S26. EIS plots of NIF for HER at different PO_4^{3-} concentrations.

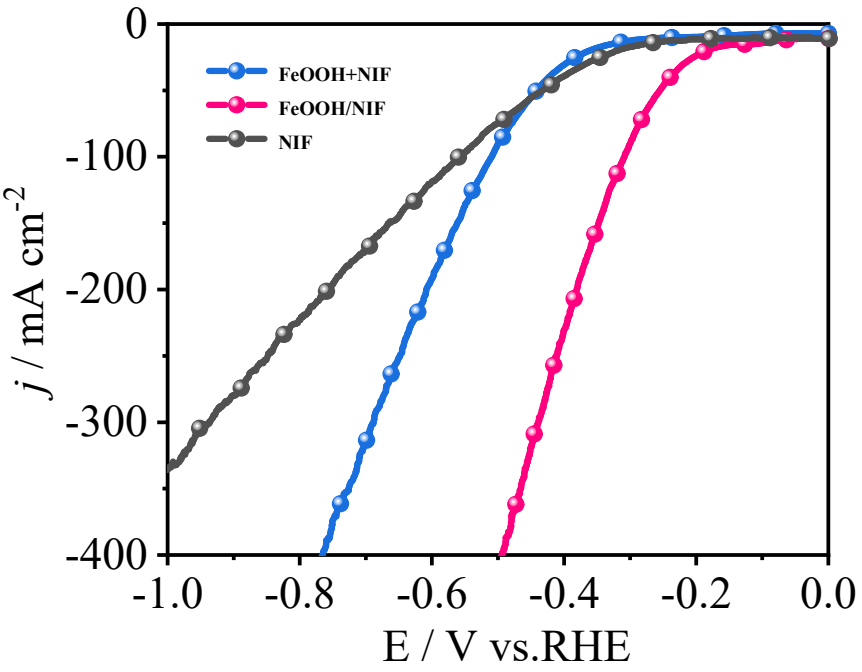

Figure S27. Comparison of LSV curves for HER for FeOOH/NIF and FeOOH+NIF in 0.10 M PO_4^{3-} + 1.0 M KOH.

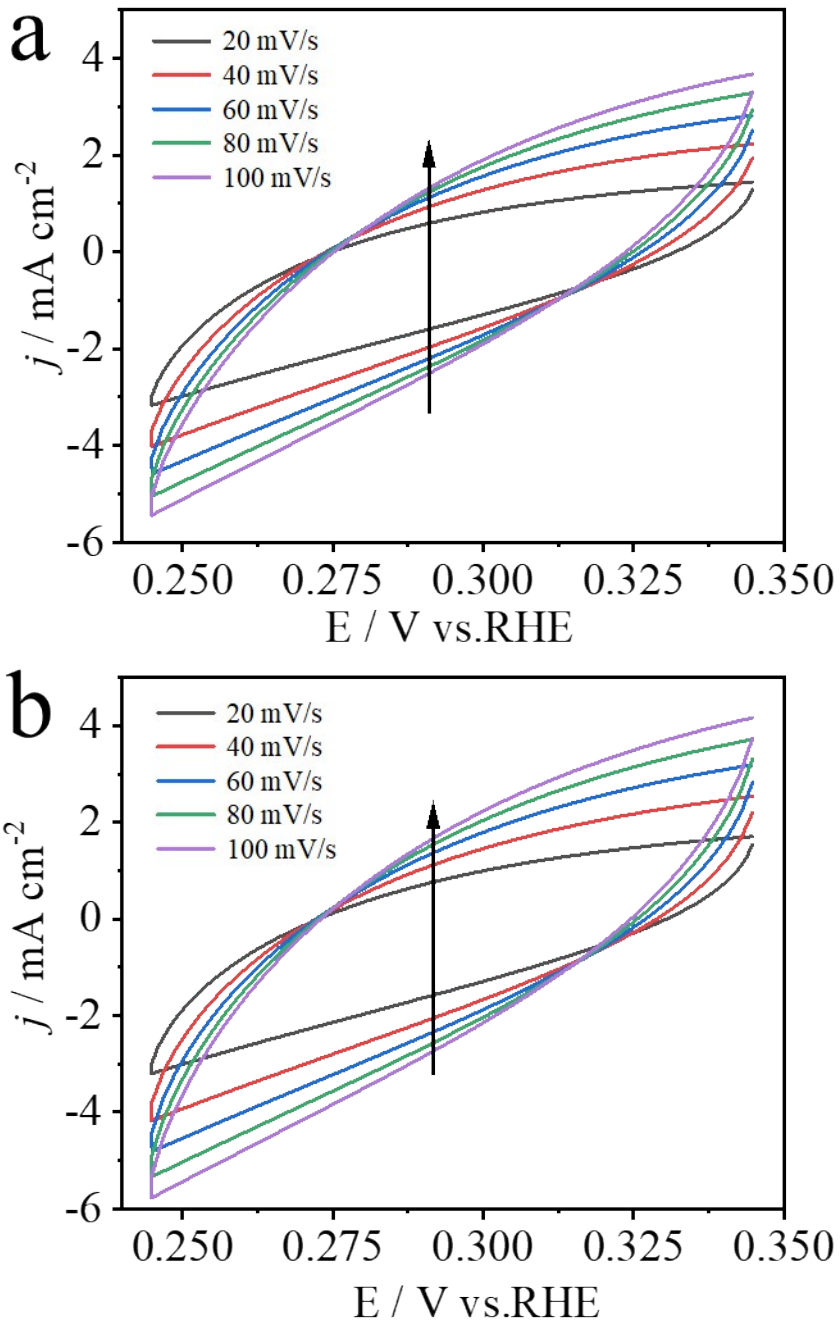

Figure S28. CV curves of FeOOH/NIF electrodes at different scan rates from 20 to 100 mV s^{-1} in (a) pure KOH, (b) 0.10 M PO_4^{3-}+1.0 M KOH.

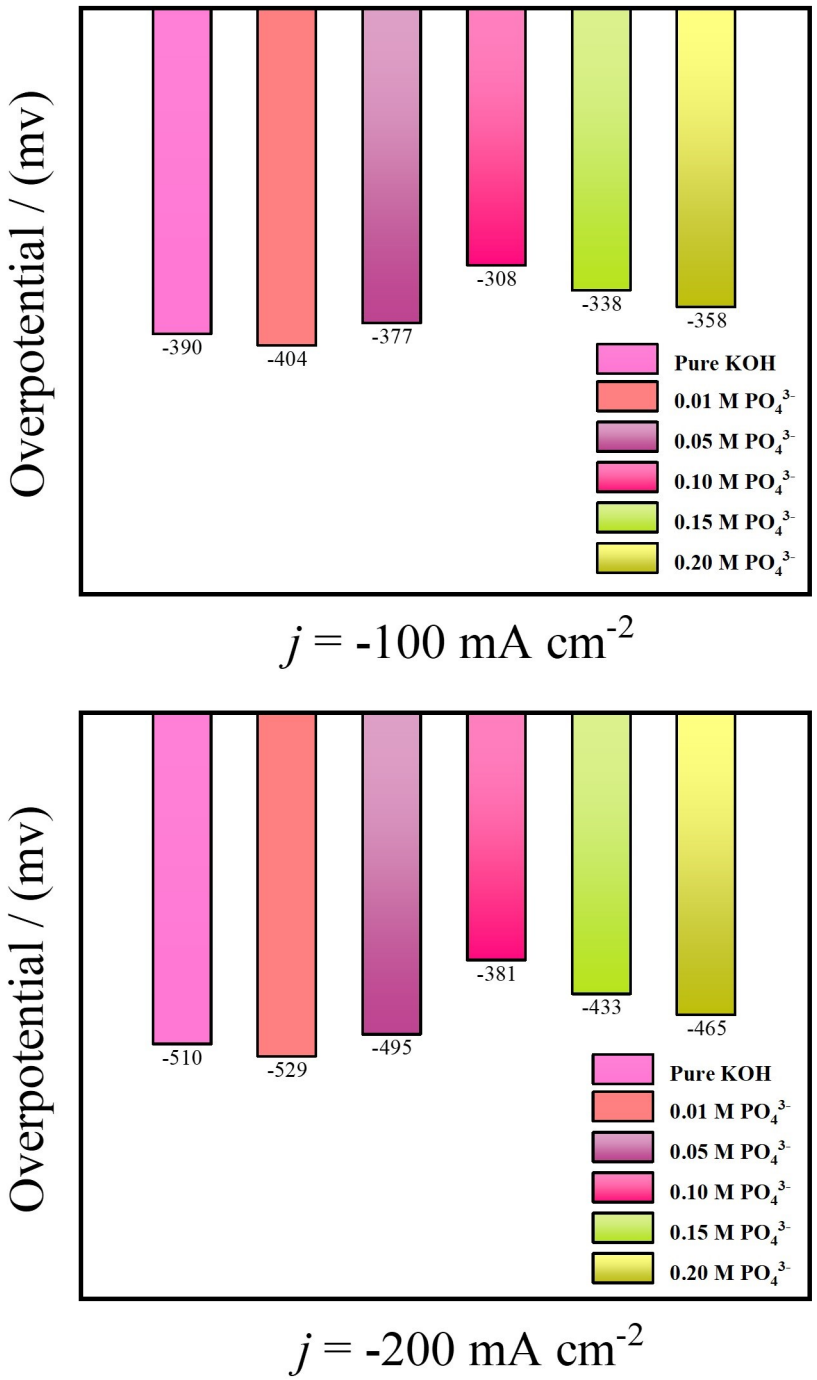

Figure S29. Comparison of FeOOH/NIF overpotentials at different PO_4^{3-} concentrations at -100 mA cm^{-2} and -200 mA cm^{-2}.

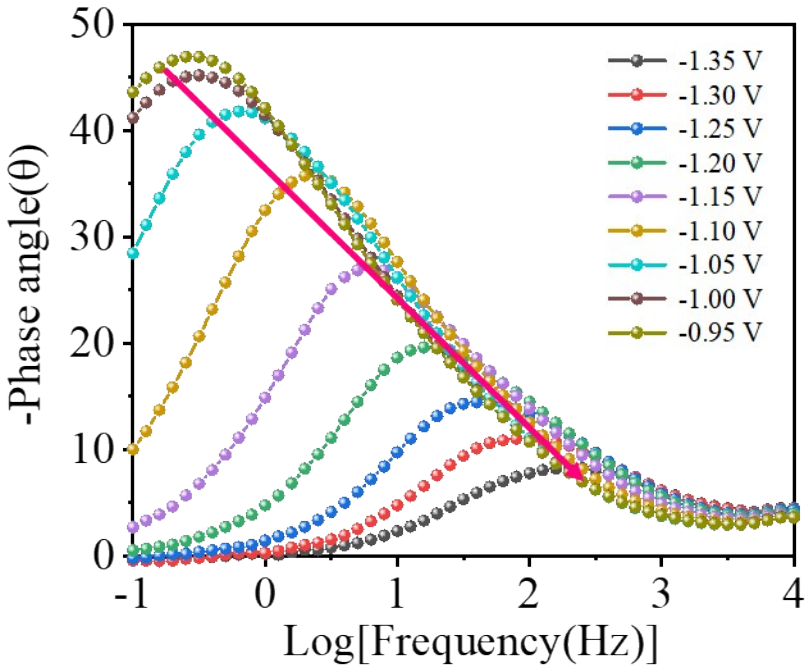

Figure S30. Bode phase plots of the FeOOH/NIF at various potentials in pure KOH.

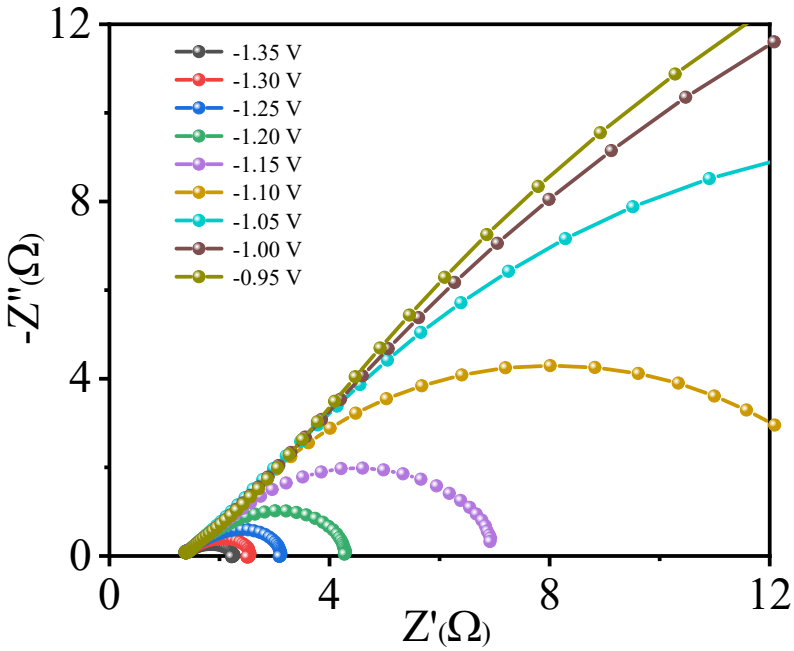

Figure S31. Operando Nyquist plots of the FeOOH/NIF at various potentials in pure KOH.

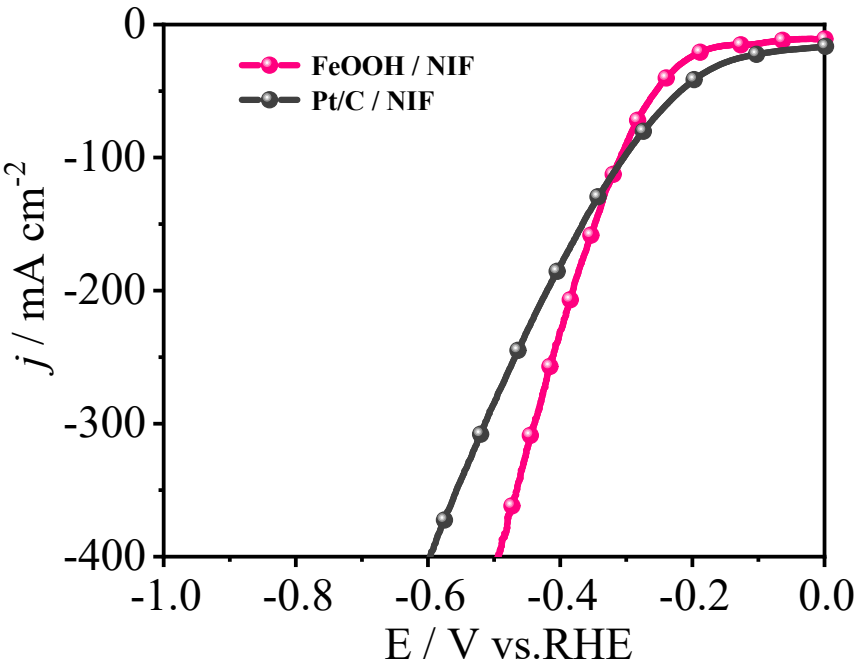

Figure S32. Comparison of LSV curves for HER between FeOOH/NIF and commercial catalyst Pt/C/NIF.

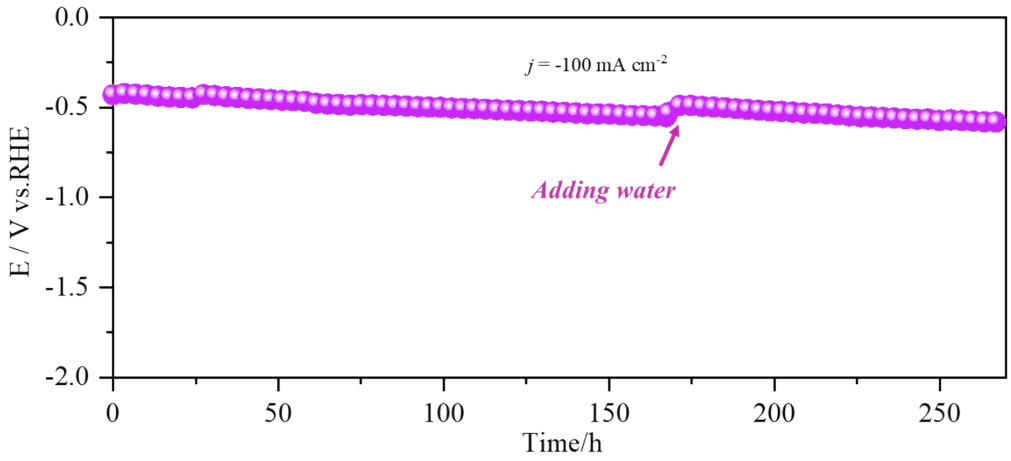

Figure S33. The long-time E-t curve of the FeOOH/NIF in 0.10 M PO_4^{3-}+1.0 M KOH for HER (j=-100 mA cm^{-2}).

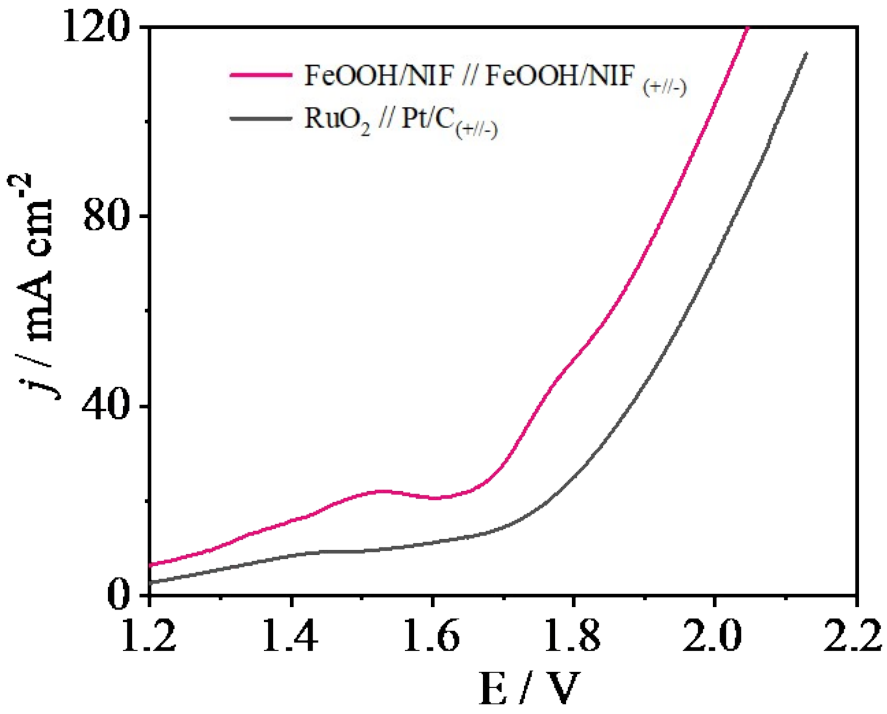

Figure S34. LSV plots of the FeOOH/NIF || FeOOH/NIF and RuO_2 || Pt/C for overall alkaline water splitting.

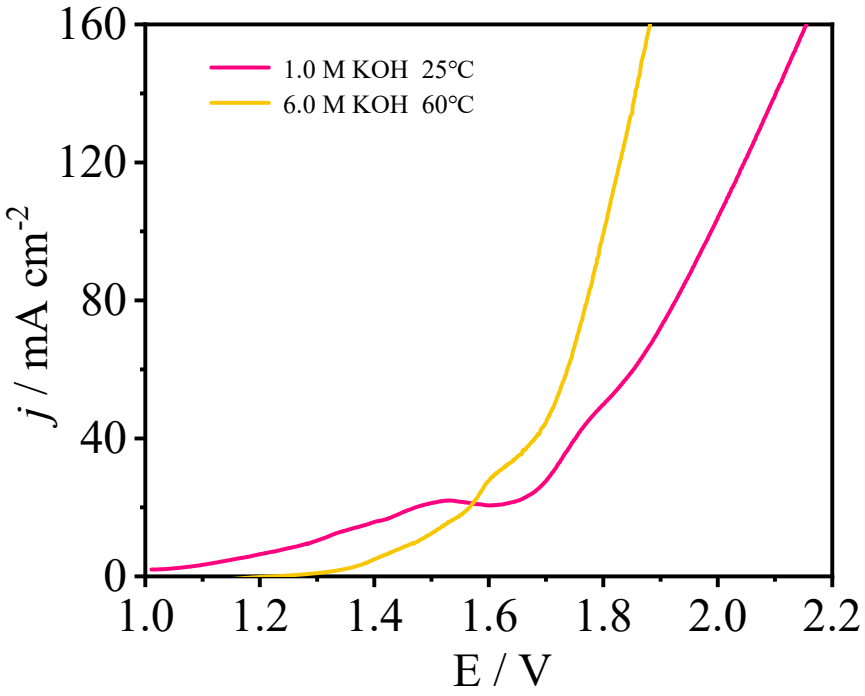

Figure S35. Comparison of LSV curves of FeOOH/NIF || FeOOH/NIF in 1.0 M KOH at 25 °C and 6.0 M KOH at 60 °C for overall alkaline water splitting.

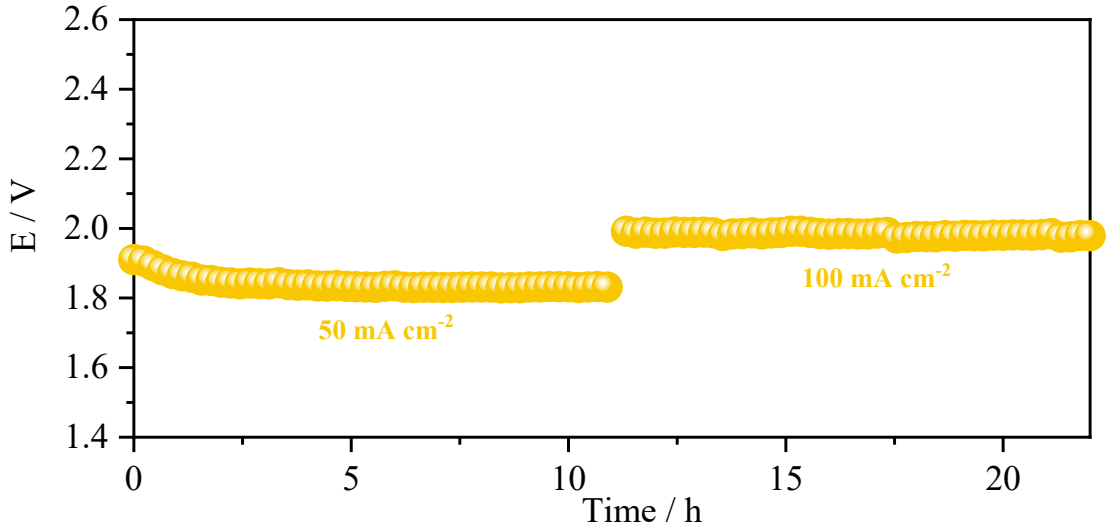

Figure S36. E-t curve of the FeOOH/NIF || FeOOH/NIF electrodes for overall water splitting at 50, 100mA cm^{-2} in 6.0 M KOH electrolyte at 60 °C.

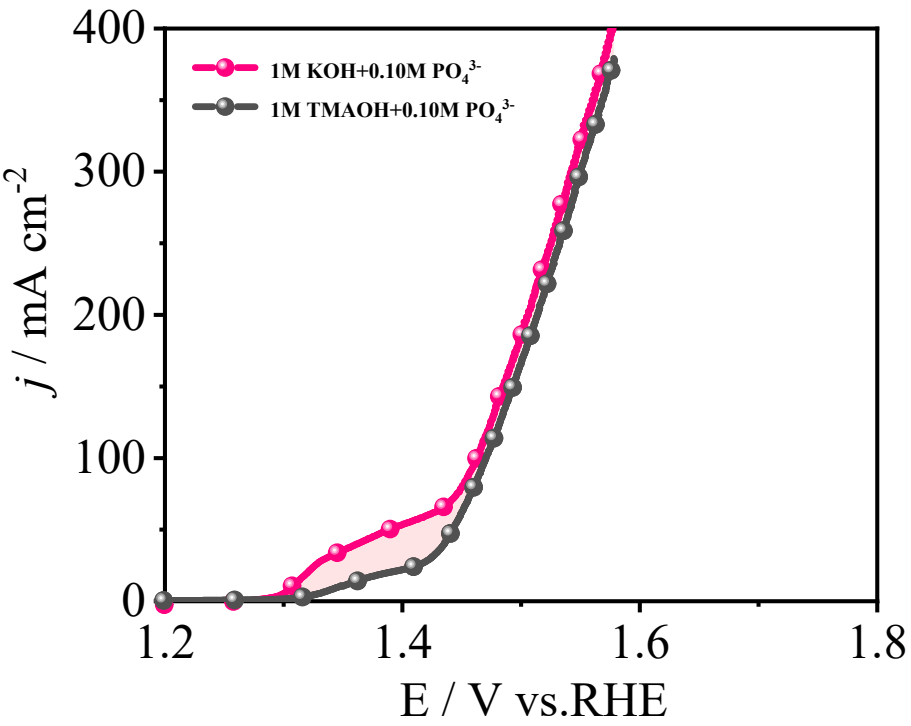

Figure S37. LSV curves of FeOOH/NIF in 1.0 M KOH+0.10 M PO_4^{3-} and 1.0 M TMAOH+0.10 M PO_4^{3-}.

In the LOM pathway, the reaction at the catalyst surface is a dynamic process. This involves oxidizing, exchanging, and liberating lattice oxygen ligands on the catalyst's exterior. These reactions usually involve the participation of oxygen-containing substances ($*O_2^{2-}$ or $*O_2^{-}$), which carry a negative charge. A strong electrostatic interaction exists between TMA^+ in tetramethylammonium hydroxide (TMAOH) and the oxygenated components. This results in the facile binding of TMA^+ to the oxygenated components, which in turn competes with the OER, thus inhibiting the OER reaction.

TMAOH was employed as an electrolyte to monitor the oxygenated substances throughout the reaction, utilizing TMA^+ as an electron probe. From the figure, it was evident that the performance of the electrode exhibited minimal change after the addition of TMAOH, suggesting that the reaction mechanism of the OER for FeOOH/NIF was not LOM. This approach provided indirect evidence that the OER reaction was AEM mechanism.

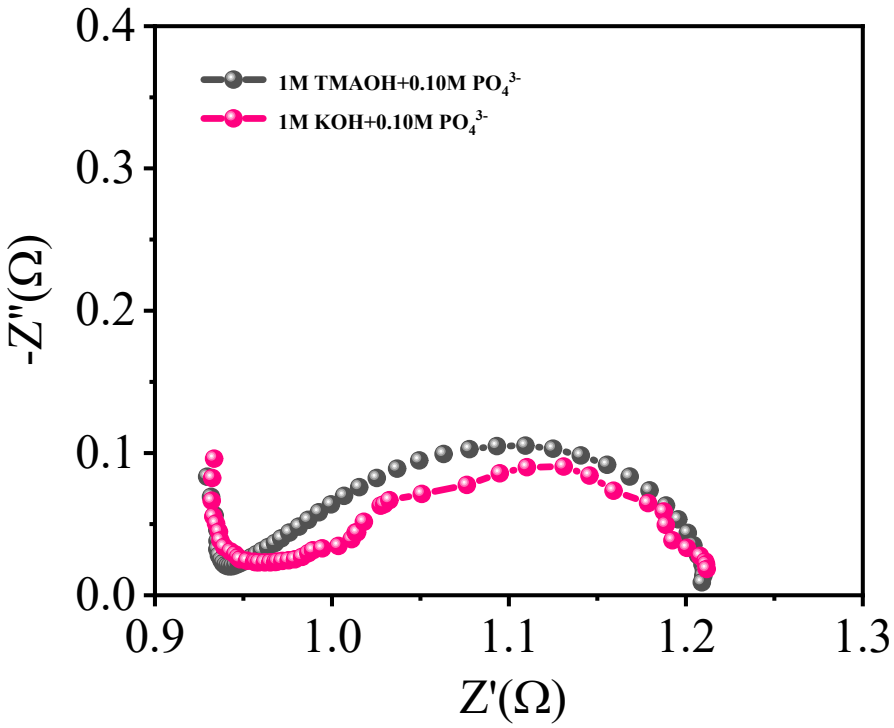

Figure S38. EIS plots of FeOOH/NIF in 1.0 M KOH+0.10 M PO_4^{3-} and 1.0 M TMAOH+0.10 M PO_4^{3-}.

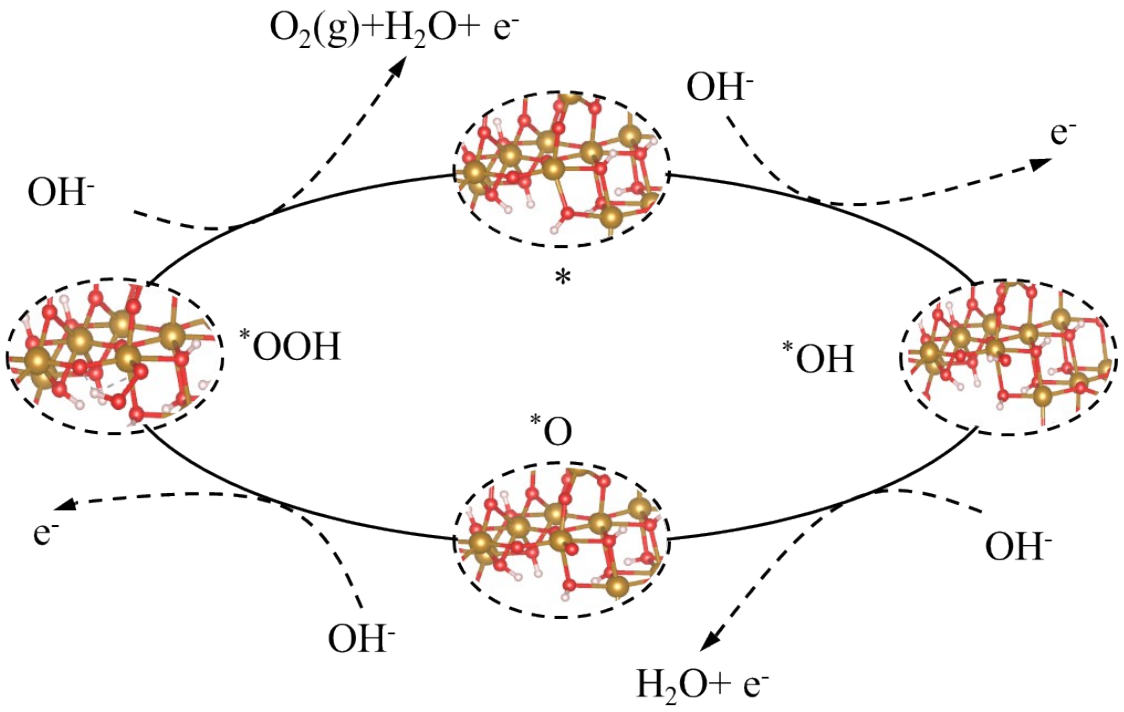

Figure S39. OER mechanism of FeOOH at Fe sites.

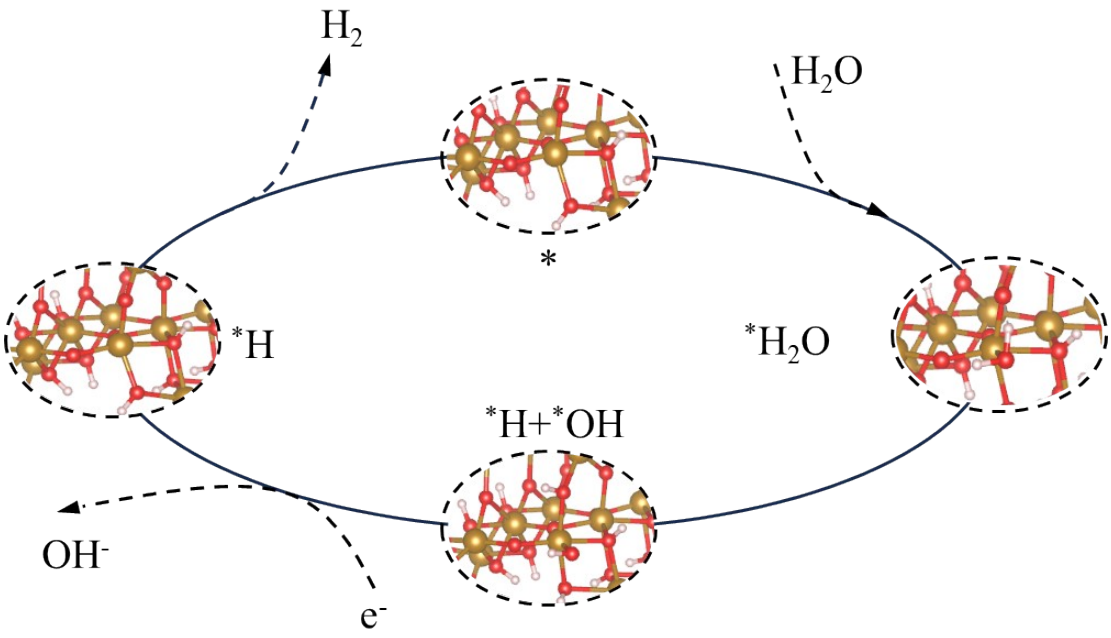

Figure S40. HER mechanism of FeOOH at Fe sites.

3. Supplementary Tables

Table S1. Comparison of OER performance of the as-prepared catalysts in this study with those reported in the literature.

Chemisorbed oxyanions	Electrocatalysts	OER Overpotential(mV)	Electrolyte	Ref.
PO_4^{3-}	FeOOH/NIF	η_{100} of 232	1.0 M KOH+0.10 M PO_4^{3-}	This work
SO_4^{2-}	Ni_2Fe-LDH/$FeNi_2S_4$/NF	η_{100} of 240	1.0 M KOH	6
SO_4^{2-}	NF-S0.15	η_{100} of 247	1.0 M KOH	7
NO_3^-	$Co_{0.15}$-NiNH	η_{100} of 255	1.0 M KOH	8
CrO_4^{2-}	NiFe-LDH/NF	η_{100} of 273	1.0 M KOH + 0.10 M CrO_4^{2-}+ seawater	9
SO_4^{2-}	NiFe-LDH	η_{100} of 274	1.0 M KOH + 0.50 M NaCl + 0.05 M Na_2SO4	10
SO_4^{2-}	R-CoNiPS	η_{100} of 300	1.0 M KOH	11
MO_4^{2-}	FeCoNiCrMo/HEA	η_{100} of 303	1.0 M KOH	12
MO_4^{2-}	FeMo-NiP_x/NF	η_{100} of 303	1.0 M KOH + seawater	13
/	HEPS	η_{100} of 313	1.0 M KOH + seawater	14
SO_4^{2-}	NiS-NF	η_{100} of 335	1.0 M KOH	15

Table S2. Comparison of HER performance of the as-prepared catalysts in this study with those reported in the literature.

Electrocatalysts	HER Overpotential(mV)	Electrolyte	Ref.
FeOOH/NIF	η_{100} of 298	1.0 M KOH+0.10 M PO_4^{3-}	This work
$Co_5Mo_{1.0}P$/NSs@NF	η_{100} of 300	1.0 M KOH	16
2Co-NC-700	η_{10} of 303	1.0 M KOH	17
$NiMoO_4$-S_x	η_{100} of 306	1.0 M KOH	18
$CoCo_2O_4$/N, Co-C-900	η_{100} of 313	1.0 M KOH	19
$Co_{5.47}$N@N-rGO-750	η_{100} of 320	1.0 M KOH	20
0.5Co-Mo-O@C	η_{10} of 323	1.0 M KOH	21
$NiCo_2O_4$	η_{100} of 335	1.0 M KOH	22
Co-HNC	η_{100} of 350	0.1 M KOH	23
$NiMoO_4$	η_{100} of 378	1.0 M KOH	18
Co/CoP-NC	η_{100} of 380	0.1 M KOH	23
$Ni_{0.1}Co_{0.9}$-MOF	η_{100} of 512	1.0 M KOH	24

Table S3. Raman band positions and shoulders (sh) of FeOOH/NIF in the region 200~1000 cm^{-1}.

Crystalline phase	Band positions(cm^{-1})	
	OER	
	1.0 M KOH	1.0 M KOH+0.10 M PO_4^{3-}
β-FeOOH	307, 395, 526, 700	308, 390, 530, 710
α/β-FeOOH	312, 475, 552, 703	308, 470, 550, 710
	HER	
β-FeOOH	394, 440, 501, 540, 674,	390, 505, 670
β/δ-FeOOH	277, 377, 501, 598, 686	270, 370, 500, 600, 690

4. References

1. X.Q. Du, J.J. Zhang, X.Y. Zhou, M.Y. Zhang, N.L. Wang, X. Lin, P.F. Zhang and Z.H. Luo, *Green Chemistry*, 2025, **27**, 3515-3523.
2. J.J. Zhang, W.W. Bao, M.Y. Li, C.M. Yang and N.N. Zhang, *Chem. Commun.*, 2020, **56**, 14713-14716.
3. G. Kresse and D. Joubert, *Phys. Rev. B*, 1999, **59**, 1758-1775.
4. J.P. Perdew, K. Burke and M. Ernzerhof, *Phys. Rev. Lett.*, 1996, **77**, 3865-3868.
5. G. Kresse and J. Furthmüller, *Phys. Rev. B*, 1996, **54**, 11169-11186.
6. L. Tan, J.T. Yu, C. Wang, H.F. Wang, X.E. Liu, H.T. Gao, L.T. Xin, D.Z. Liu, W.G. Hou and T.R. Zhan, *Adv. Funct. Mater.*, 2022, **32**, 2200951.
7. H.X. Liao, T. Luo, P.F. Tan, K.J. Chen, L.L. Lu, Y. Liu, M. Liu and J. Pan, *Adv. Funct. Mater.*, 2021, **31**, 2102772.
8. Y.N. Zhou, F.T. Li, B. Dong and Y.M. Chai, *Energy Environ. Sci.*, 2024, **17**, 1468-1481.
9. L. Ye, Y. Ding, X.Q. Niu, X.Y. Xu, K.C. Fan, Y.H. Wen, L.B. Zong, X.W. Li, X.F. Du and T.R. Zhan, *J. Colloid Interface Sci.*, 2024, **665**, 240-251.
10. T.F. Ma, W.W. Xu, B.R. Li, X. Chen, J.J. Zhao, S.S. Wan, K. Jiang, S.X. Zhang, Z.F. Wang, Z.Q. Tian, Z.Y. Lu and L. Chen, *Angew. Chem. Int. Ed.*, 2021, **60**, 22740-22744.
11. F.T. Luo, P. Yu, J.T. Xiang, J.J. Jiang and S.J. Chen, *J. Energy Chem.*, 2024, **94**, 508-516.
12. L.Y. Yi, S.M. Xiao, Y.P. Wei, D.Z. Li, R.F. Wang, S.F. Guo and W.H. Hu, *Chem. Eng. J.*, 2023, **469**, 144015.
13. J.S. Zhou, L.H. Liu, H.X. Ren, L.M. Li, W. Song, N. Li, X.X. Shi, C.D. Kou, Y.T. Sun, M. Han, H.B. Wang, J.R. Han, K.N. Liu, C.D. Momo, Y.Y. Liu, D.H. Feng, W.J. Zhu, S.H. Chen, H. Jiang, Y.C. Liu and H.Y. Liang, *Inorg. Chem. Front.*, 2024, **11**, 498-507.
14. Y. Dai, X.Y. Tu, K.H. Yue, Y.J. Wan, P. Zhao, X.R. Shi, F.Q. Huang and Y. Yan, *Adv. Funct. Mater.*, 2025, **35**, 2417211.
15. H.X. Xu, K. Li, N. Liu, W. Xia, W.H. Liu, D. Cao, L.P. Zhang and D.J. Cheng, *Catal. Sci. Technol.*, 2023, **13**, 6780-6791.
16. Y. Zhang, Q. Shao, S. Long and X.Q. Huang, *Nano Energy*, 2018, **45**, 448-455.
17. J.J. Lv, P.L. Hu, J.Q. Zheng, S.C. Mo, W.P. Liu, S.Z. Chen and Y.J. Liu, *J. Power Sources*, 2024, **602**, 234339.
18. C. Hu, T.T. Wang, L. Chen, Q. Xue, J.W. Feng, X.J. Liu, X.X. Ma, D.L. Wang, J. Wu, P. He, Y.L. Guo and H.Y. Ni, *Electrocatalysis*, 2025, **16**, 106-116.
19. A.J. Wang, X. Yang, F.Q. Zhang, Q.T. Peng, X.Y. Zhai and W.H. Zhu, *Dalton Trans.*, 2024, **53**, 14725-14734.
20. X.X. Shu, S. Chen, S. Chen, W. Pan and J.T. Zhang, *Carbon*, 2020, **157**, 234-243.
21. L. Gong, K. Lan, X. Wang, X.K. Huang, P.B. Jiang, K.Z. Wang, M. Yang, L. Ma and R. Li, *Int. J. Hydrogen Energy*, 2020, **45**, 544-552.
22. C. Zhang, J.M. Wang, Y. Liu, W.P. Li, Y.L. Wang, G.H. Qin and Z.G. Lv, *Chemistry-An Asian Journal*, 2022, **17**, e202200377.
23. Y.C. Hao, Y.Q. Xu, W. Liu and X.M. Sun, *Mater. Horiz.*, 2018, **5**, 108-115.
24. J.J. Cai, Z.C. Xu, X.X. Tang, H. Liu, X.Y. Zhang, H.J. Li, J.M. Wang and S. Li, *J. Alloys Compd.*, 2023, **947**, 169498.